The Dissertation Committee for Qingwei Mo certifies that this is the approved version of the following dissertation:

Vertical Cavity Surface Emitting Laser Based on

GaAs/Air-gap Distributed Bragg Reflectors:

From Concept to Working Devices

Committee:

_____

Dennis G. Deppe, Supervisor

_____

Dean P. Neikirk

_____

Jack C. Lee

_____

Ananth Dodabalapur

_____

John G. Ekerdt

Vertical Cavity Surface Emitting Laser Based on

GaAs/Air-gap Distributed Bragg Reflectors:

From concept to Working Devices

by

Qingwei Mo, B.E., M.S.E

Dissertation

Presented to the Faculty of the Graduate School of

the University of Texas at Austin

in Partial Fulfillment

of the Requirements

for the Degree of

Doctor of Philosophy

The University of Texas at Austin

December 2004

To my grandmother, Gao Yanyun,

my parents, Mo Yunda and Gao Shunrong,

and my wife, Peng Weiping

Acknowledgements

Vertical Cavity Surface Emitting Laser Based on

GaAs/Air-gap Distributed Bragg Reflectors:

From concept to Working Devices

Qingwei Mo, Ph.D.
The University of Texas at Austin, 2004

Supervisor: Dennis G. Deppe

Vertical-cavity surface-emitting lasers (VCSELs) have created new opportunities in optoelectronics. However, VCSELs have so far been commercialized mainly for operation at 0.85 μm, despite their potential importance at other wavelengths, such as 1.3 μm and 1.55 μm. The limitations at these longer wavelengths come from material characteristics, such as a low contrast ratio in mirror materials, lower mirror reflectivity, and smaller optical gain for longer wavelength materials versus AlGaAs/GaAs quantum wells. A similar situation, insufficient gain relative to the cavity loss, existed in the past for shorter wavelength VCSELs before high quality epitaxial mirrors were developed. Semiconductor/air-gap Distributed Bragg Reflectors (DBRs) are attractive due to their high index contrast, which leads to a high reflectivity, wide stop band and low optical loss mirror with a small number of pairs. This concept is ready to be integrated into material systems other than AlGaAs/GaAs, which is studied in this work. Therefore, the

impact of these DBRs can be extended into both visible and longer infrared wavelengths as a solution to the trade-off between DBR and active region materials. Air-gap DBRs can also be used as basic building blocks of micro-opto-electro-mechanical systems (MOEMS). The high Q microcavity formed by the air-gap DBRs also provide a good platform for microcavity physics study.

Air-gap DBRs are modeled using the transmission matrix formulae of the Maxwell equations. A comparison to existing DBR technology shows the great advantage and potential that the air-gap DBR possesses. Two types of air-gap are proposed and developed. The first one includes multiple GaAs/air pairs while the second one combines a single air-gap with metal and dielectric mirrors. New device structures and processing designs, especially an all-epitaxial lateral current and optical confinement technique, are carried out to incorporate air-gap DBRs into VCSEL structures. The first VCSEL based on a GaAs/air-gap DBR is successfully demonstrated. Low threshold continuous-wave lasing is achieved at room temperature. The device characteristics and air-gap DBR loss are analyzed based on experimental data.

Table of Contents

Chapter 1

Introduction

1.1 VCSEL Basics

The Vertical Cavity Surface Emitting Laser (VCSEL) was first proposed by Prof. Kenichi Iga in 1977 at the Tokyo Institute of Technology[1]. It has been extensively studied in the following decades because of the interests in both the applications and fundamental physics. The basic physics governing the operation of VCSELs is the same as other types of diode lasers. The optical gain is provided by stimulated emission via electrical current injected into the active region. The optical cavity formed by mirrors in some fashion provides the necessary feedback to sustain the laser oscillation. However, the geometry of the VCSEL is substantially different from conventional edge-emitting lasers. The vertical cavity is formed by multi-epitaxial layers and the optical output is taken from one of the mirror surfaces as shown in Figure.1.1.

The original motivation for VCSEL development was a fully monolithic fabrication of the laser cavity. However, this unique structure turns out to offer a lot more than that. The advantages identified so far include: 1) on-wafer testing performed before dicing which reduces the cost of chip production; 2) easy coupling to an optical fiber due to

good mode matching between the circular beam shape and optical fiber core; 3) formation of densely packed and precisely arranged 2-D arrays; 4) ultra-low threshold operation due to its small cavity and active region volume; 5) large relaxation frequencies which enables the high-speed modulation; 6) a vertical stack structure that provides the capability to be integrated with micromachining technology, which will be discussed in detail later in this dissertation; 7) compatibility with VLSI technology, which promises to be a potential building block for future Optoelectronic Integrated Circuits (OEIC).
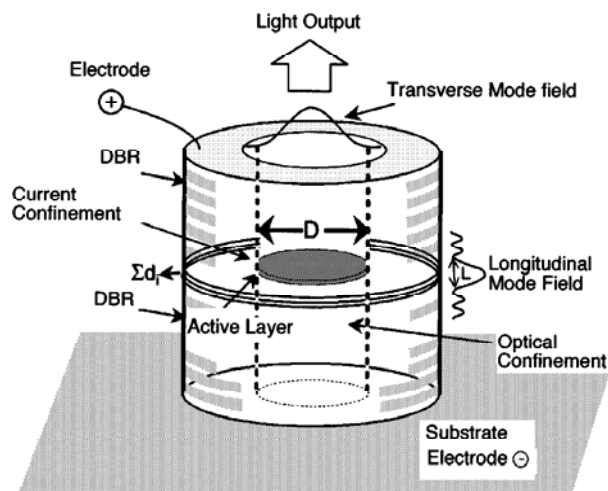
Figure 1.1 Basic structure of VCSEL[2]

VCSELs started being commercialized after the inception of IEEE and Fiber Channel standard for high-speed data communication in 1997. Since then, more than 30 million VCSELs have been shipped for this application alone[3]. Besides this major application in optical communication, VCSELs penetrate into many non-communication

2

markets because of its unique merits. The 2-D array VCSELs are ideal for high resolution

laser printers. The low power consumption makes them an ideal solution for many

hand-held applications including bar-code scanners. They have also been used in

proximity sensing and optical encoding due to their simple optical requirements and

wavelength controllability. Red VCSELs operating at 650nm are playing an increasingly

critical role in plastic optical fiber (POF) of the automobile and aerospace internal data

transfer network. A novel laser scanning display based on a VCSEL array has also been

demonstrated, indicating a promising future in the huge display market[4].

1.2 Devices designs and challenges
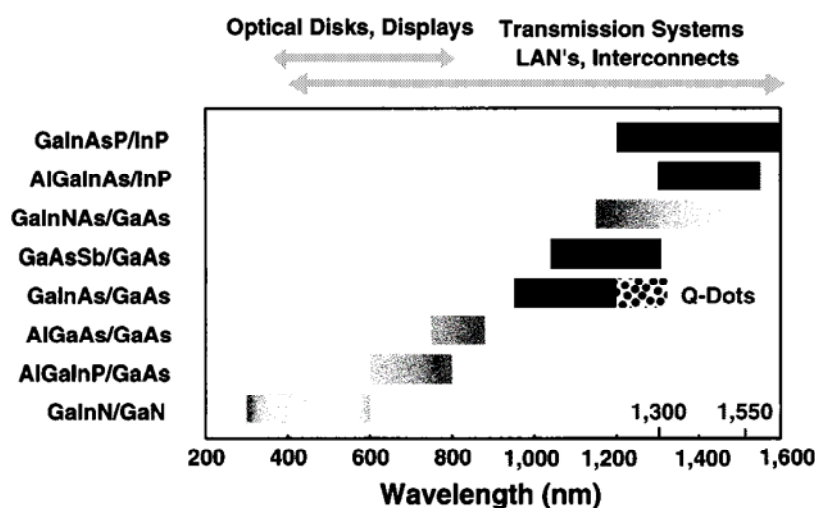
Figure 1.2 materials for VCSELs[2]

Although the generic structure of a VCSEL consists of only two parallel reflectors

and a thin active region sandwiched between them, the design and development of a

VCSEL involves materials science, semiconductor physics and electromagnetics.
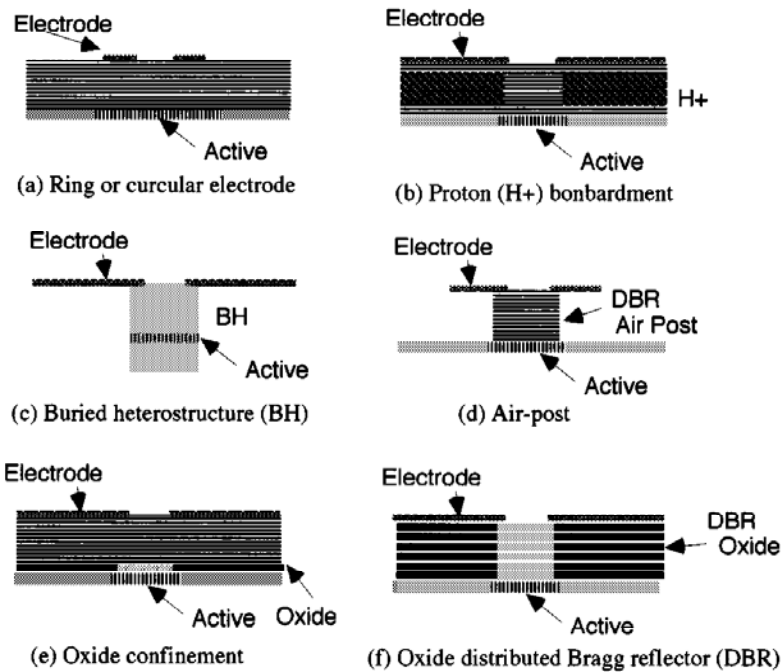
Figure 1.3 current confinement schemes[2]

Firstly, to achieve the operation at a specific wavelength, the right active material must be chosen and grown with high quality. Figure 1.2 shows different material candidates for various wavelengths and applications. Secondly, high quality reflectors must be grown on both sides with material that is lattice-matched with the rest of the cavity. The typical reflectivity of a VCSEL mirror is higher than 99.9%. Most VCSELs use DBRs as mirrors to provide optical feedback. DBR technology and its compatibility with the active region materials will be the major topic of Chapter 2. Thirdly, the confinement of the current and lasing mode into a small volume is necessary to achieve lasing operation. Several schemes for current confinement have been proposed and developed, as shown in Figure

1.3. Figure 1.3(a) is a simple ring structure, which is very easy to build but cannot confine the current effectively. Figure 1.3(b) is a proton implantation technique that is used in a lot of commercialized devices. In Figure1.3(c), the mesa and active region is buried in a wide band-gap material. This is an ideal structure but hard to build. An air post is etched in Figure 1.3(d) for confinement, which may cause nonradiative recombination. In Figure 1.3(e) and Figure 1.3(f), Al(Ga)As layers either inside the cavity or in the DBR are converted into AlOx, which provide both current confinement, due to its insulating properties and optical confinement, due to its smaller refractive index. This is a major milestone of VCSEL development for achieving efficient, low threshold operation[5,6]. In this dissertation, another all-epitaxial current and optical confinement scheme is demonstrated. It eased the process integration with air-gap DBRs in this work and has a very promising future because of its advantages and flexibility. This technique will be described in detail in Chapter 3.

The development of qualified active region materials and high quality DBRs has been challenging. Integrating these two features without generating high defect densities or exorbitant costs is even more difficult. This is the main obstacle hindering the extension of VCSEL wavelengths from 780nm, 850nm and 980nm to longer and shorter wavelengths. The primary motivation for this work is to solve this problem by developing a novel DBR technology, with concepts and principles that can easily be applied to

different material platforms and wavelengths.

1.3 Motivation

There are three major motivations for developing this air-gap DBR technology and integrating it with VCSELs. First, it is a promising solution to the trade-off between the active region and DBR material quality. Previously, we always have to sacrifice one for the other. Secondly, it marries micromachined structures with VCSELs, which may add new features and controllability to these devices. Third, a high Q optical cavity with small mode volume can be employed as a platform for studying microcavity electrodynamics (QED).

The development of the 1.3μm VCSEL is a good example to illustrate the dilemma of active region versus DBR material quality. VCSELs operating at 1.3μm have been touted for a long time due to their low dispersion transmission in optical fibers. However, commercialization of these devices has not been achieved until recently[7]. Table 1.1 shows the approaches that have been pursued. InGaAsP/InP can be grown monolithically on InP substrate, but suffers from a low refractive index contrast between InGaAsP and InP. InGaAs quantum dots[8], GaAsSb[9], and GaInNAs[10] have gained a lot of attention, because they can take advantage of the mature AlGaAs/GaAs DBR technology. However, more research is needed to improve the gain and stability of these materials. Another approach is to bond the AlGaAs/GaAs DBRs to an InGaAsP cavity[11]. This has achieved good

6

performance, but is questioned for the manufacturability and cost. Doubtlessly, this dilemma will continue to hinder the endeavors to push VCSELs into 1.55μm or the visible spectrum. Air-gap DBRs can potentially be used in these different material platforms monolithically and provide high reflectivity to the devices.

Active region	DBR	Challenges
InGaAsP	InGaAsP/InP	Low Index contrast
InAs Quantum Dots	AlGaAs/GaAs	Low material gain
InGaAsP	AlGaAs/GaAs (Bonding)	Manufacturability
GaAsSb	AlGaAs/GaAs	Gain blue shift
GaInNAs	AlGaAs/GaAs	Gain and reliability

.   Table 1.1 Approaches for 1.3μm VCSEL

The integration of micromachined structures with VCSELs opens the way to combine active optoelectronic devices with micro-mechanical functions and develop new generation smart devices. Existing and future applications include tunable VCSELs[12], highly selective and widely tunable Fabry-Pérot filters[13], wide-band optical switchs, selective and tunable detectors[14], etc. The MBE or MOCVD grown compound semiconductor structure also offers superior flexibility and precision for micromachining.

7

The surface quality and built-in strain can be controlled to realize very fine and complex geometries and configurations.

Air-gap DBRs may also play a critical role in microcavity physics research. As indicated by Purcell in 1946[15], Microcavities have a fundamental impact on the spontaneous recombination process described by Equation 1.1[16],

$$\frac{1}{\tau_{sp}} = \frac{\alpha_{wg}}{\tau_{sp,0}} + \frac{1}{\tau_{sp,0}} \cdot \frac{2\omega^2(\frac{c}{n})^3}{\omega_0^4 V} \cdot \frac{(\gamma + \frac{\omega_0}{Q_0})\exp(-(x^2 + y^2)/w_0^2)}{(\omega_0 - \omega)^2 + (\frac{\gamma}{2} + \frac{\omega_0}{2Q_0})} \qquad \text{(Equation. 1.1)}$$

Where $\tau_{sp,0}$ is the cavity free spontaneous emission lifetime, V is mode volume, ω and ω_0 are the frequency of the emitter and microcavity respectively, γ is the emitter dephasing rate, Q_0 is the photon loss rate of the cavity mode , and w_0 is the lateral size of the confined optical mode. α_{wg} is the coupling into the waveguide, which does not change much over free emission. The impact of an air-gap DBR is present in two aspects of this equation. It increases Q due to high reflectivity and shrinks the mode volume V due to the small penetration depth, resulting from a large refractive index contrast.

1.4 Dissertation Outline

This dissertation will present the author's study on air-gap based VCSELs. This research has gone through the procedures of device modeling, process development, process

integration, device demonstration and device analysis. The same procedure is followed in writing this dissertation. After the introduction of VCSEL technology and motivation for these projects in Chapter 1, air-gap DBR modeling and process development are presented in Chapter 2. Process integration is discussed in Chapter 3 followed by the demonstration of VCSEL lasing operation. Chapter 3 concludes with analysis and discussion of the performance of the VCSELs observed during development. Chapter 4 summarizes the dissertation.

Chapter 2

Air-gap Distributed Bragg Reflectors:

Theory and Micromachining

2.1 DBR modeling

VCSELs need mirrors with high reflectivity, usually >99%, due to a short gain region. Most VCSELs employ Distributed Bragg Reflectors as shown in Figure 2.1. Quarter wavelength thick layers of two different index materials are alternated during growth. The concept is that many small reflections can add up to a large reflection. When the electromagnetic field in the cavity is at the Bragg frequency, the reflection at each interface will add up in phase with each other and generate a very high reflectivity.
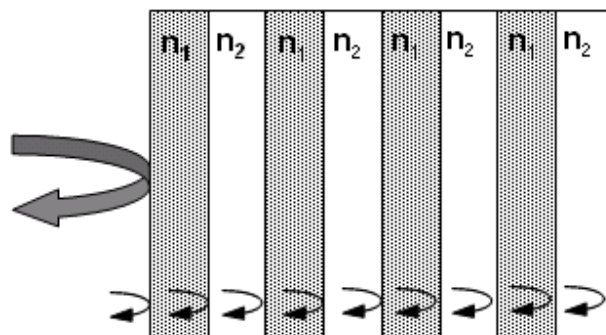
Figure 2.1 Schematic of a DBR structure

One elegant way to model a DBR is to use transmission matrix formulation of Maxwell's equations[17], which is the approach used in this work. One transmission matrix is used to express the normalized amplitudes relationship between the input and output at a given port in terms of the other ports. Therefore, one network shown in Figure 2.2 can be expressed by Equation. 2.1.

$$\begin{bmatrix} A_1 \\ B_1 \end{bmatrix} = \begin{bmatrix} T_{11} & T_{12} \\ T_{21} & T_{22} \end{bmatrix} \begin{bmatrix} A_2 \\ B_2 \end{bmatrix}$$

Equation 2.1
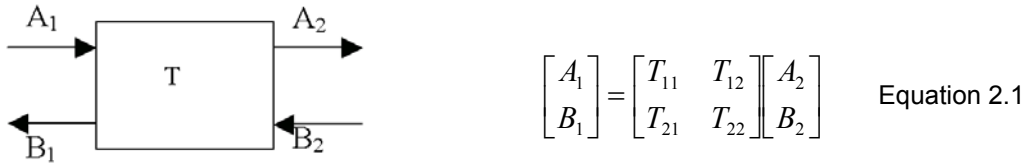
Figure 2.2 Single two-port network

$$\begin{bmatrix} A_1 \\ B_1 \end{bmatrix} = \frac{1}{t_{12}} \begin{bmatrix} 1 & -r_{21} \\ r_{12} & t_{12}t_{21} - r_{12}r_{21} \end{bmatrix} \begin{bmatrix} A_2 \\ B_2 \end{bmatrix}$$

Equation 2.1

Figure 2.3 Network for DBR interface

$$\begin{bmatrix} A_1 \\ B_1 \end{bmatrix} = \begin{bmatrix} e^{j\tilde{\beta}L} & 0 \\ 0 & e^{-j\tilde{\beta}L} \end{bmatrix} \begin{bmatrix} A_2 \\ B_2 \end{bmatrix}$$

Equation 2.2

Figure 2.4 Network for each layer inside

11

In this way, a multilayer DBR or even a complete optical cavity can be divided down to two basic components: the dielectric segment and the interface of refractive index discontinuity. These two building blocks and their transmission matrix are illustrated in Figure 2.3 and 2.4, respectively. In Equation 2.2, r and t represent r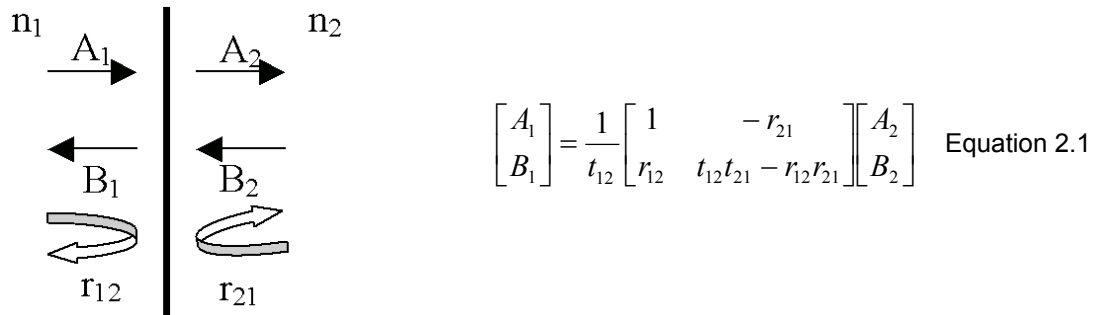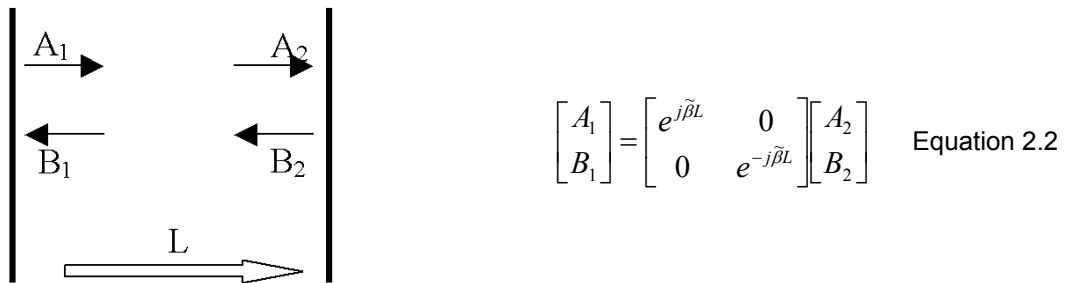eflectivity and transmission, respectively. $\tilde{\beta}$ in Equation 2.3 is the complex propagation constant which includes loss, gain and the phase change of the electromagnetic field. Therefore, multiple DBR layers can be modeled by multiplying the matrix of each component. A typical DBR reflectivity curve and that of a complete VCSEL cavity is shown in Figure 2.5. As indicated in Figure 2.5(a), there is a regime of wavelength where the reflectivity is very high. It is the stop-band of the dielectric stack. There is a dip in the stop-band of the complete VCSEL structure, which reveals the axial mode of the Fabry-Pérot cavity. The transmission matrix can also be used to calculate the electromagnetic field distribution inside the cavity. In order to maximize the optical gain, the active region should be placed at the antinodes of the electromagnetic field inside the cavity. The E-field distribution of a typical 980nm VCSEL with GaAs/AlAs DBR is shown in Figure 2.6. The interface of each epitaxial layer is indicated by the periodic short vertical lines. The numerical simulation also reveals the relationship between high/low index order, cavity length, and the position of antinodes/nodes inside the cavity. Four configurations with different index ordering and cavity length are shown in Figure 2.7.
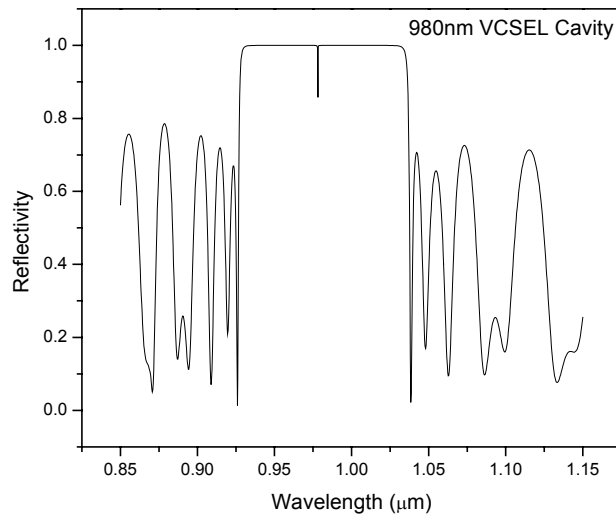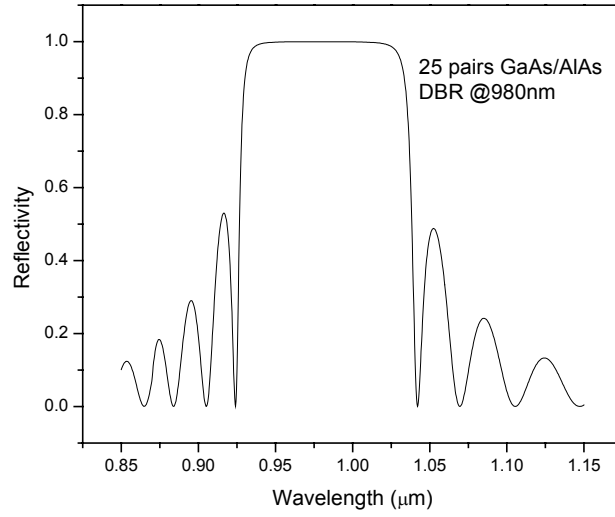
Figure 2.5 (a) Reflectivity of a typical GaAs DBR
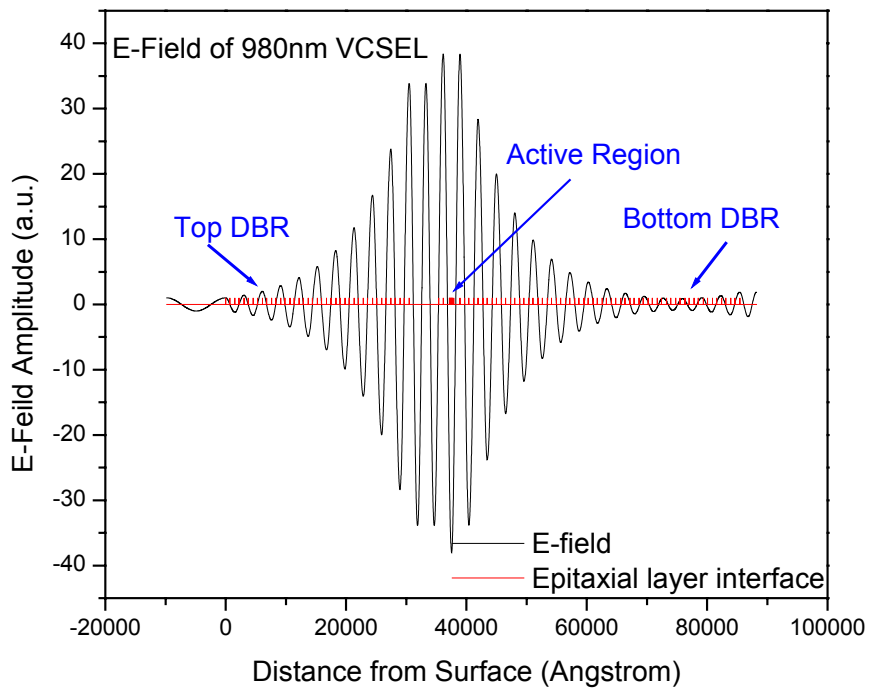(b) Reflectivity of a complete 980 VCSEL cavity

13

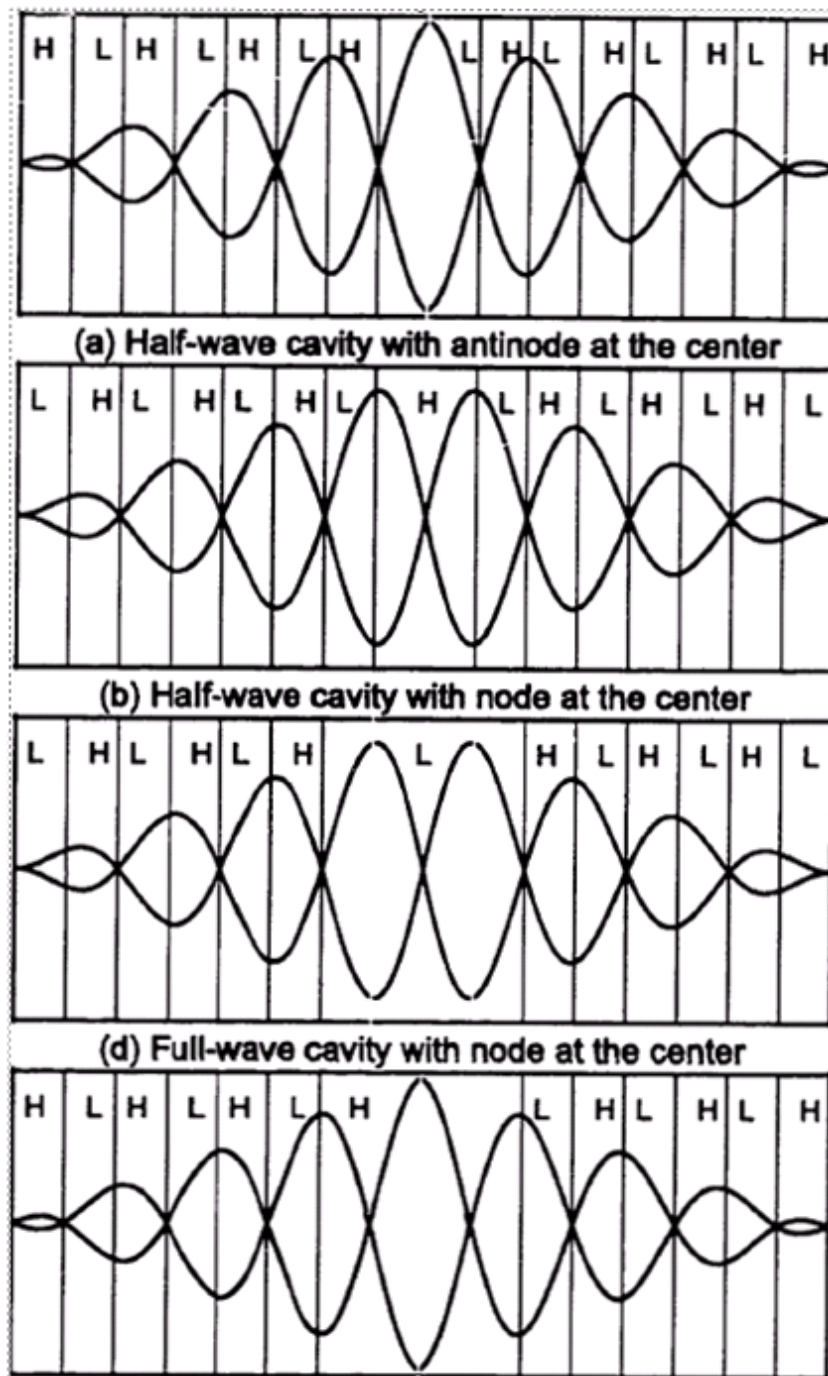Figure 2.6 E-Field of 980nm VCSEL

Figure 2.7 Configuration of Index high/low ordering, cavity length
and antinodes/nodes position[18]

The numeric calculation based on the transmission matrix of Maxwell's equations gives satisfying results and serves as a powerful tool in VCSEL DBR and cavity design. However, the simplified analytic model with appropriate approximations reveals underlying physics and insights into the properties of these dielectric stacks. When the Bragg condition is met in a lossless dielectric stack, and the reflectivity at each interface is small, the total reflectivity of the DBR can be reduced to Equation 2.4 or more generally, to Equation 2.5^{17}, where n_1 and n_2 (n_{Li}, n_{Hi}) are the alternating indices of the dielectric stack, and m is the total number of pairs. Equation 2.4 is plotted in Figure 2.8, showing that the more pairs achieve a higher r, which agrees with intuition. Also, the higher the index contrast, the fewer number of DBRs needed to reach the same reflectivity. Air-gap DBR can provide highest index contrast to any material system, which also brings the advantages such as lower absorption loss and serial resistance. Furthermore, with the same assumption of lossless material and small reflectivity at each interface, the reflectivity ratio between m pairs DBR and that of one single pair, m_{eff}, denotes the effective number of periods seen by the incident field. When multiplied by the period ($L_1 + L_2$), m_{eff} determines the penetration depth of the field into the dielectric stack. Minimizing the penetration depth is a critical step for confining the photons into a small volume for microcavity physics research. It also helps to suppress lateral diffraction loss. As shown in Equation 2.6 and 2.7, high index contrast can effectively decrease the

16

penetration depth. Another important parameter in DRB design is the stop band. A wide stop-band translates to a slow phase change on the reflection. The flatter the phase change, the smaller the resonance shifting when the epitaxial layer thickness of the VCSEL deviates from the design number. This can be described by Equation 2.9[19], where L is the cavity length, n is the cavity effective refractive index, λ_{res} is the VCSEL resonant frequency, and Φ_a, Φ_b are the phase change of the top and bottom DBRs, respectively. Detailed modeling of air-gap DBR and a comparison to existing technology will be discussed in the next section.

Reflectivity vs. Index contrast
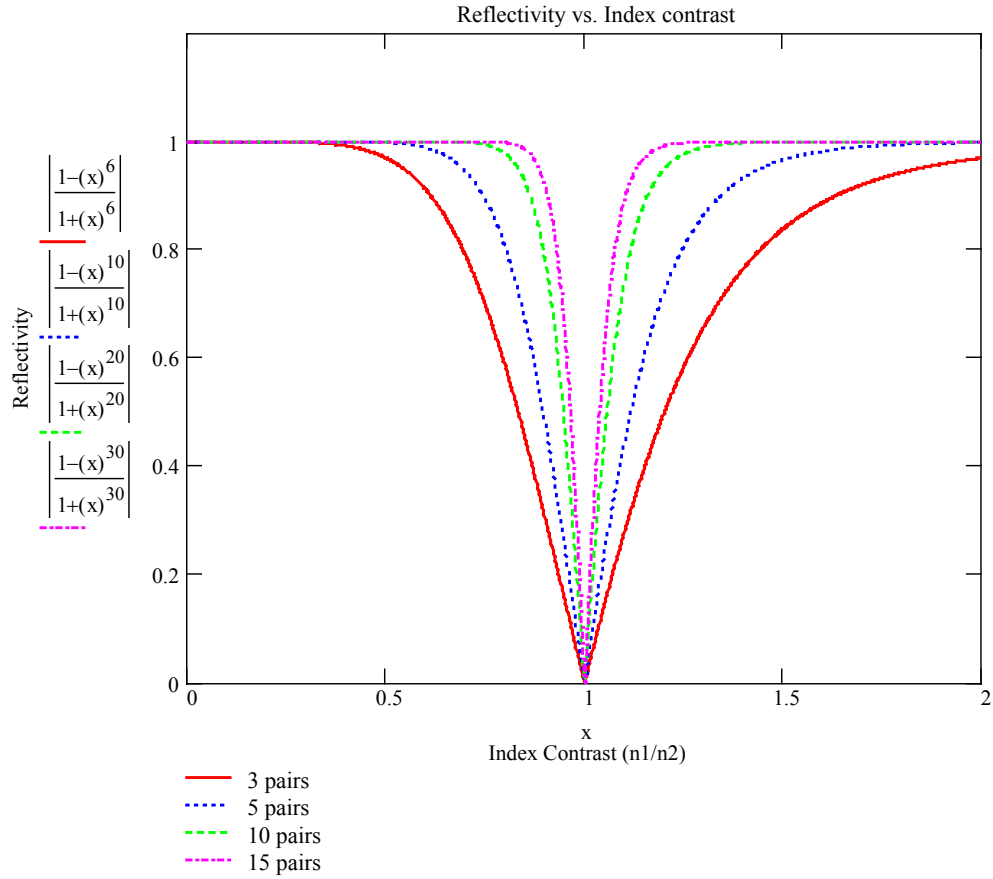
Figure 2.8 DBR reflectivity vs. index contrast and number of pairs

$$r = \frac{1 - \left(\dfrac{n_1}{n_2}\right)^{2m}}{1 + \left(\dfrac{n_1}{n_2}\right)^{2m}}$$

Equation 2.3

$$r = \frac{1 - \displaystyle\prod_{0}^{N}\left[\dfrac{n_{Li}}{n_{Hi}}\right]}{1 + \displaystyle\prod_{0}^{N}\left[\dfrac{n_{Li}}{n_{Hi}}\right]}$$

Equation 2.4

$$m_{eff} = \frac{\tanh\left[m\ln\left(\frac{n_2}{n_1}\right)\right]}{\tanh\left[\ln\left(\frac{n_2}{n_1}\right)\right]}$$ Equation 2.5

$$L_{penetration} = m_{eff}\cdot\left(L_1 + L_2\right)$$ Equation 2.6

$$\Delta\lambda_{stop-band} = \frac{2\lambda\Delta n}{\pi n_{eff}}$$ Equation 2.7

Where $n_{eff} = 2\left(\frac{1}{n_1} + \frac{1}{n_2}\right)^{-1}$

. $$\frac{2\pi n L}{\lambda_{res}} + \Phi_a + \Phi_b = 2m\pi$$ Equation 2.8

2.2 DBR Technology

One of the principal obstacles in pushing VCSEL technology into longer (1.3μm, 1.55 μm) and shorter (UV and visible) wavelengths has been the lack of high-quality DBRs that can be integrated with the active region materials emitting at these specific wavelengths. High quality here means high reflectivity, high thermal conductivity, high electrical conductivity and low optical loss. All these considerations must be balanced in order to achieve and optimize VCSEL operation.

VCSEL mirrors usually need to have reflectivity of 99% or higher, due to the short gain length. This high reflectivity is obtained by alternating high and low

refractive-index materials, which is called Distributed Bragg Reflectors (DBRs). The optical property of DBRs can by modeled using the transmission matrix of the Maxwell's equations. The analytic formulas determining the reflectivity, stop-band width and penetration depth are given by Equation 2.4-Equation 2.8.

The technologies used to build DBRs include monolithic epitaxy (MBE or MOCVD) and post-growth deposition (E-beam deposition, PECVD, sputtering, etc). The materials employed include epitaxial semiconductor films, which are lattice-matched with the substrate, post-growth deposited dielectric films (Si/SiO$_2$[20], MgF/ZnSe[21], etc) and metal reflectors (Gold, Silver, etc). Epitaxial grown semiconductor DBRs have good crystal quality and low material absorption; therefore, they can reach a very high peak reflectivity. However, they suffer from low refractive index contrast, which translates to more pairs of DBRs needed to attain a certain peak reflectivity. Taking 1.3μm as an example, InGaAsP/InP has a index contrast (δn) of 0.178 and GaAs/AlAs has a contrast of 0.22. Therefore, 65 and 22 pairs are needed to reach a peak reflectivity of 99.9%, respectively.

Post-growth deposited dielectric films can provide high index contrast. For example, MgF/ZnSe and Si/SiO$_2$ have contrasts of 1.19 and 2.15, respectively, requiring 6 and 5 pairs, respectively, for a 99.9% reflectivity. The drawback of these deposited dielectric mirrors is their amorphous structures, which have a much higher optical loss

than epitaxial semiconductor DBRs. A typical absorption coefficient for Si is α $\approx 1000cm^{-1}$ at $1.3\mu m^{22}$, while MgF/ZnSe has an α of $\sim 200cm^{-1}$. The peak reflectivity of a DBR with such high loss tends to saturate, regardless of how many additional pairs are deposited. Si/SiO_2 saturated at 0.992 after 4 pairs were deposited and MgF/ZnSe saturated at 0.997 with 7 pairs. These values are not high enough to achieve lasing for emerging active materials, such as quantum dots. Additionally, using deposited DBRs on both sides of VCSEL is challenging in processing, which involves substrate holing. Dielectric DBRs usually require complicated current injection schemes. The thermal conductivity of these dielectric mirrors is not very good either, which hinders the dissipation of heat generated during resistive and lasing operations.[23]

Native oxide converted from AlGaAs by wet thermal oxidation has been studied as a promising DBR material[19]. $GaAs/AlO_x$ has an index contrast of 1.8 at $1.3\mu m$ and can achieve a reflectivity of 99.9% with 5 pairs of mirrors. Impressive VCSEL operation has been achieved and characterized with high optical quality DBRs based on native oxide[19]. The main obstacle preventing the manufacture of this technology is the detrimental thermal strain introduced during wet thermal oxidation. This strain may cause reliability issues in devices based on this technology.

Metal reflectors have a long history in VCSEL development, since the very first VCSEL devices were realized[24]. Gold and Silver are usually used, because they have a

fairly high reflectivity (>95%) in the desired spectrum. The reflectivity at the surface of a metal reflector can be derived by solving Maxell's equations. There will be an extra phase shift because the good conduction properties of gold or silver. This phase shift has to be accommodated by designing an extra phase shift layer. The problem with metal reflectors is the difficulty in using them on both sides of the VCSEL cavity. It requires implementing a bottom-emitting scheme, which is not feasible in many applications.

Compared to the technologies mentioned above, air-gap DBRs enjoy many advantages. They have the largest achievable index contrast, which allows a high peak reflectivity with a minimum number of mirrors. The wide stop-band increases the cavity fabrication tolerance. Since air-gap are released from epitaxial sacrificial layers, they have an excellent interface quality and precise thickness control. Built-in strain can be controlled very well by epitaxial growth technologies. There are no limitations to the use of air-gap DBRs on both sides of the laser cavity. And extra electrical and thermal resistivity caused by the air-gap can be minimized by engineering the right scheme of sacrificial-layer etching. The last and most critical value of air-gap DBRs is the decoupling of material choice for active region and DBR, solving the dilemma of material compatibility between these two components. Any combination of semiconductor material can be used, regardless of the index contrast, as long as they can be monolithically grown with the active region and substrate and a selective etching

method, with a reasonably high selectivity, can be found between them. Those layers selected as sacrificial layers can always be etched away to form high contrast and high reflectivity DBRs. Table 2.1 lists the comparisons between existing DBR technologies and air-gap based DBR, in terms of index contrast, number of pairs required for 99.9% reflectivity, stop-band width and final DBR thickness. Figure 2.9 shows the reflectivity modeling results of air-gap based DBRs compared to conventional GaAs/AlAs pairs with the same reflectivity.

1.3 μm DBR materials	$\delta n = n_h - n_l$	#of pairs for 99.9%	Bandwidth (nm)	Thickness (μm)
InGaAsP/InP	0.178	65	50	13
GaAs/AlAs	0.46	22	120	4.5
MgF2/ZnSe	1.19	6	710	2.2
GaAs/AlO	1.81	5	797	1.5
GaAs/Air [$\lambda/4$]	2.41	3	1433	1.3
GaAs/Air [$3\lambda/4$]	2.41	3	561	1.8
GaAs/Air [$5\lambda/4$]	2.41	3	245	2.4

Table 2.1 1.3μm DBR technology
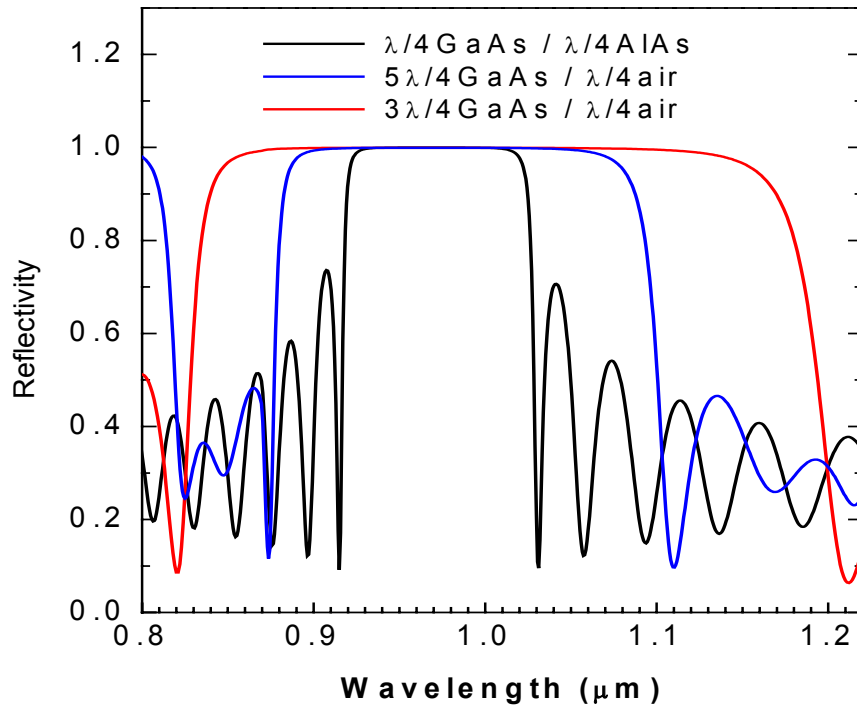
Figure 2.9 stop-band width of 980nm DBR based
on GaAs/AlAs and GaAs/Air with similar reflectivity

2.3 Proposed Air-gap DBR structures

Structure I: Air-gap DBRs

Structure II: Hybrid DBRs with Air-gap and metal mirror
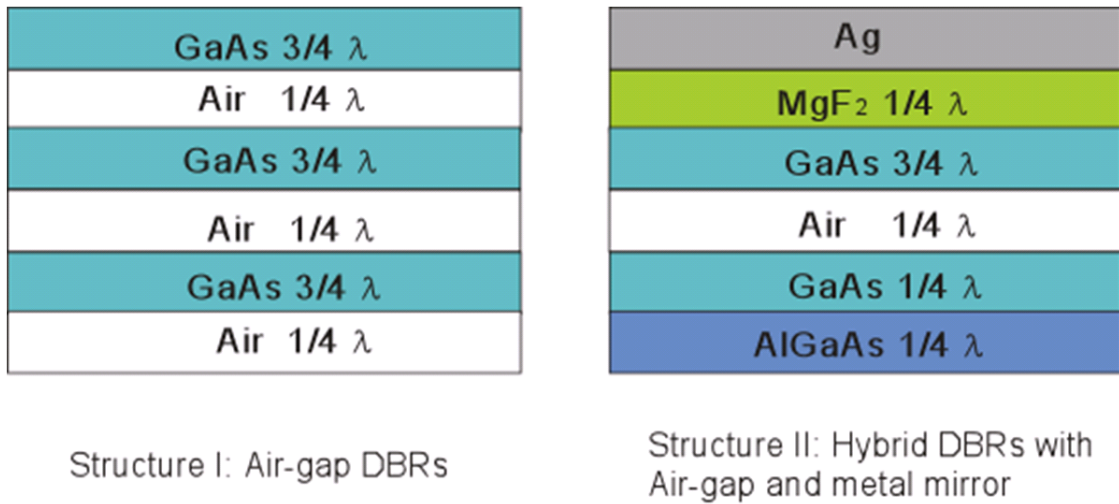
Figure 2.10 two proposed air-gap DBR structure

There are two air-gap based structures proposed in this dissertation research. Structure I is a pure air-gap solution, which stacks three pairs of GaAs/air-gap together. It simplified the processing steps and is ready to be used on both the top and bottom of VCSELs. Intuitively, more air-gaps should be more challenging to process; however, we eventually found that this is not the case. A three quarter wavelength thickness was for GaAs in order to enhance mechanical stability. Structure II is a hybrid solution combining one air-gap with a post-growth dielectric film and a silver reflector. It is more robust, and the silver reflector contributes to a high reflectivity and mechanical support sufficient for

the suspended structure and the potentially current and thermal path for the VCSEL operation. However, this design involves more processing steps and makes process integration more difficult. It is also only suitable for one side of the cavity, which limits its applications. Transmission matrix modeling has been carried out for both structures. The reflectivity and final thickness of these two structures are also presented and compared to GaAs/AlAs and MgF/ZnSe pairs in Figure 2.11.

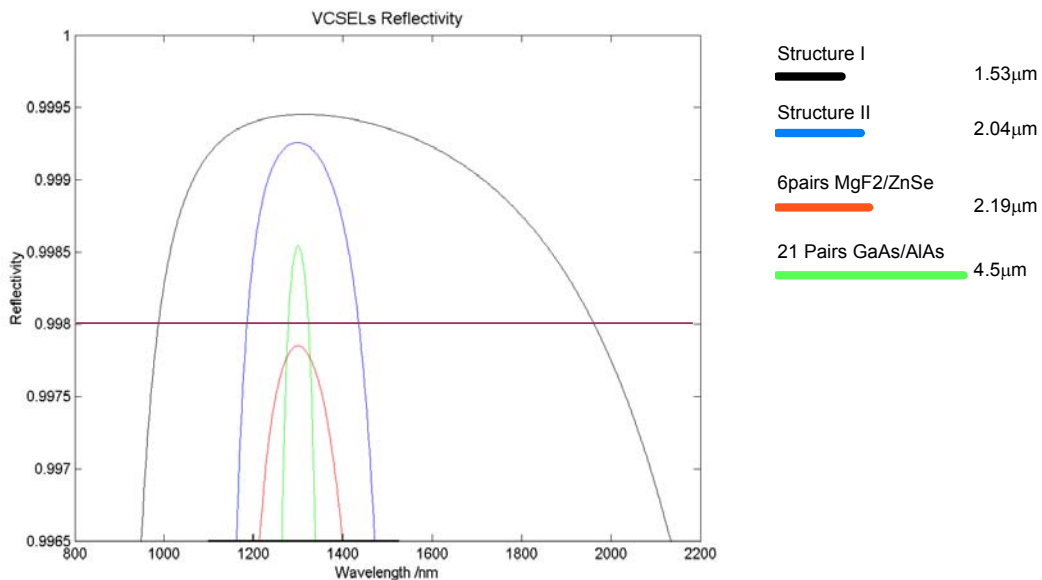

Figure 2.11 comparison of reflectivity and final thickness between structure I, II and conventional DBRs

2.4 Development of Air-gap DBRs

This work focused on developing a simple, robust, and high yield fabrication process to incorporate air-gap technology to GaAs-based VCSEL manufacturing. Two different structures are proposed in 2.2.3. Process flows have been developed for these two

26

structures. Both of them are based on a sacrificial layer etching technique, which is a typical surface micromachining processing. What is unusual in this work is the extremely small air-gap and suspended thickness, which is ~2000-3000 Angstrom, while a typical Si MEMS structure is several to tens of microns. A notorious problem in surface micromachining is the permanent attachment of the suspended structure to the layer underneath, which is called sticking or stiction.[25,26,27,28,29,30] Sacrificial layers are usually etched away using a wet chemical etching technique, because in most cases only a wet etching can an provide effective undercut[31].

During drying, after the rinse, the capillary force induced by the diminishing liquid will pull the suspended layer down. Many theories have been proposed to explain the permanent stiction, which include etch residues,[25,26] electrostatic forces,[27] Van der Waals forces and hydrogen bridging[28,29].   Therefore, this work focused on solving this problem by engineering the mechanical structure design, selective etching process, rinse and drying techniques. Many techniques have been developed to prevent stiction. Most of them fall into two categories. The first group of methods is to prevent the pulling down by freeze drying,[32] critical point drying,[33] dry etching techniques[31], or temporary or permanent mechanical supporting structures[34]. The second group reduces the adhesion force and enables the suspended structure to recover from the physical contact by using its own restorative force. These methods include minimizing the surface energy,[26] reducing the

27

contact area by using a bump or increasing the surface roughness.[35,36]

2.4.1 Type I Air-Gap DBR development

2.4.1.1 Stiction Problems
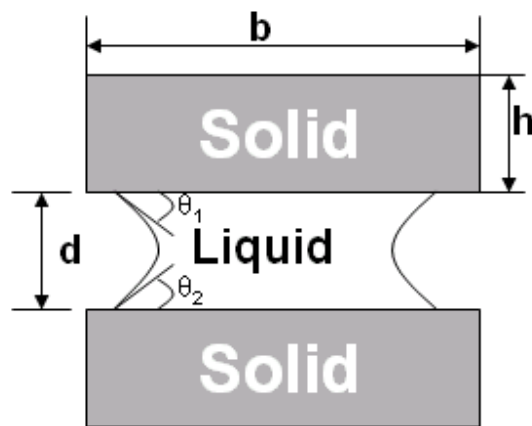
Figure 2.12 Cross section of suspended structure when drying

There are two phases from rinse and dry to stiction. The first step is the pull-in phase, in which the suspended structure is pulled down to the underlying layer by capillary force. The second step is the adhesion phase, in which an adhesion mechanism starts dominating and prevents the suspended structure from recovering even after all the water is gone. In the phase one, the mechanism is very much like the electrostatic attraction between two charged parallel plates. The surface tension of the liquid causes the pull-in force to bring

the film down, while the bending stiffness of the suspended structure tries to recover it. When the deflection of the beam increases, both the capillary force of the liquid and spring force of the beam increase. If the equilibrium between these two forces is broken by the capillary force increasing at a faster rate, the suspended structure will eventually fall down and physically touch the layer underneath, as shown in figure 2.13.

The pull-in length is used to characterize this behavior, which denotes the longest free-standing clamped-clamped beams without being totally pulled down. It can be modeled by Equation 2.9 when ignoring the built-in strain[37]:

$$L_p = 1.059 \left[\frac{8\hat{E}d^2h^3}{\gamma(\cos\theta_1 + \cos\theta_2)} \right]^{\frac{1}{4}} \qquad \text{Equation 2.9}$$

where $\hat{E} = E/(1-\nu^2)$ is the modulus of the material. E and ν are Young's modulus and Poisson's ratio, respectively. θ_1 and θ_2 are the contact angles between the liquid and solid as in Figure 2.12. γ is the surface tension of the liquid used for rinsing, and d and h are the thickness of the air-gap and suspended film, respectively. Plug in the material parameters of GaAs thin film, where E=8.59*10^{11}dyn/cm^2, ν=0.31, θ_1, θ_2 are 0 when pulled down, γ of water is 73dyn/cm. The thickness of air-gap and suspended film are 3250Å and 2857Å at 1.3μm, respectively. L_p=11μm is calculated in this case and increases to 13μm when water is replaced with Acetone (γ=24dyn/cm). The size budget is tight considering that the typical current aperture of a VCSEL is around 10μm. This model is very instructive in the structure and processing design. It is evident that L_p is proportional to d$^{1/2}$ and h$^{3/4}$. Thus,

we chose 3 quarter wavelength for the GaAs layer thickness to enhance the stiffness of the mirror. This demonstrates that the resistivity to pull-in is independent of the width of the bridge. L_p is also inversely proportional to the surface tension of the rinse liquid, making Acetone a better choice than water. For a high quality air-gap mirror, the suspended GaAs layers should stay perfectly flat to give high reflectivity. Therefore, this pull-down recovery cycle should be avoided even when the materials are able to recover. Critical point drying thus looks very promising, because it decreases γ nearly to zero and minimizes the bending of the bridge during the rinse and dry phases. This is also the essential technique employed to develop the type I air-gap DBR.

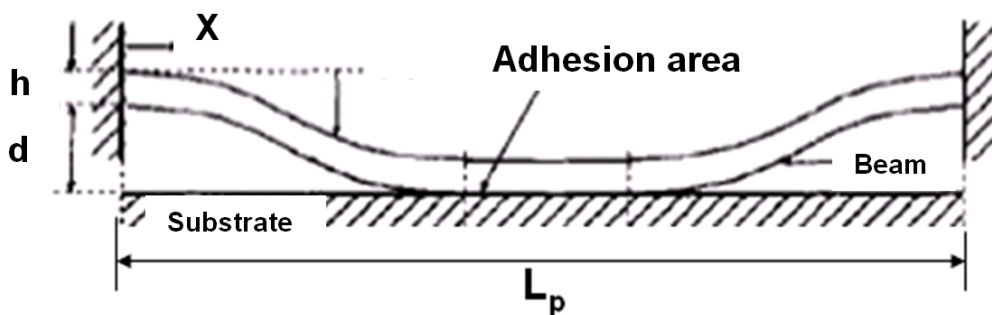Figure 2.13 Clamped-Clamped structure pulled down by capillary force

Following the pull-down phase is the adhesion phase. Different models are developed to explain the interactions between solids, which induce adhesion. Long-range mechanisms including capillary forces, van der Waals forces and electrostatic forces are among them. Short-range mechanisms include hydrogen bonds, chemical bonds and

30

metallic bonds[37]. Based on these theories, different solutions are proposed. Among them is an anti-stiction surface treatment or coating, a stand-off bump to limit the contact area, an increased surface roughness, etc. However, considering the uniqueness and high optical quality requirements for VCSEL devices, these methods are not applicable.

2.4.1.2 Critical Point Drying

Surface Tension

The critical point phenomenon was first discovered by French baron Charles Cagniard de La Tour in 1821 when he observed the disappearance of the gas/liquid interface of carbon dioxide in a sealed gun. This actually exhibited one of the fundamental natures of the transition between the vapor and liquid phase. This particular point is characterized by a fixed temperature, pressure and density, at which the distinction between the gas and the liquid phase simply disappears. As we discussed in 2.4.1.1, the primary cause of the stiction problem is the surface tension of the liquid. The origin of the liquid surface tension is the decreasing molecular density through the interface between the liquid and vapor when the phase equilibrium is set. Thus, the molecules at the interfacial zone will experience more attraction force from inside the liquid than from outside the vapor. The surface potential therefore gets higher across the interface in the direction of the vapor. A cross section of the interface between liquid and vapor are shown in Figure 2.14

along with the molecular density and surface potential distribution. The critical point, where the density of liquid and vapor becomes the same, is favorable in micro-electro-mechanical structure (MEMS) release due to the zero surface tension. A MEMS specimen immersed in the liquid can experience a transition to a "dry" gas environment without being exposed to a liquid-vapor interface, thus avoiding the damage of surface tension.
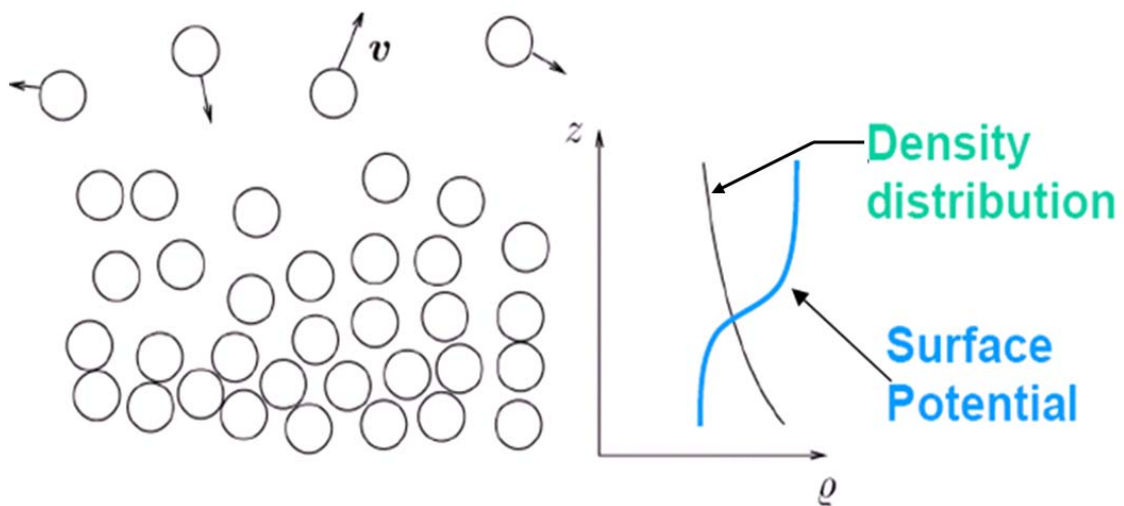

Figure 2.14 Cross section through the interface between liquid and vapor

Critical Point Drying (CPD) with CO$_2$

CRITICAL CONSTANTS		
SUBSTANCE	CRITICAL	
	TEMP. $^{\circ}$C	P.S.I.
HYDROGEN	-234.5	294
OXYGEN	-118	735
NITROGEN	-146	485
CARBON DIOXIDE	+ 31.1	1072
CARBON MONOXIDE	-141.1	528
WATER	+374	3212

Table 2.2 critical point of different material

In the experiment, liquid carbon dioxide is chosen because its critical point is comparatively easier to reach, as shown in Table 2.2, and it is also inexpensive and environmentally friendly. Figure 2.15 shows the CO$_2$ phase diagram and the typical route of CO$_2$ critical point drying. The principle of using liquid carbon dioxide is best understood by considering a group of experimental curves carried out to determine the relationship between volume and pressure at a certain temperature as shown in Figure 2.16. This type of curve is also called Isothermal.

Using the 10°C curve as an example, CO$_2$ starts from low pressure at point "R" and shrinks in volume while the pressure increases until point "S". In this range, CO$_2$ is generally considered a vapor. A slight increase of pressure after "S" leads to a large volume reduction and a transition to liquid status at "T". This is also called condensation. After "T", CO$_2$ is virtually incompressible like a typical liquid. The 20°C curve is almost

the same as 10°C one, except that the volume shrinkage is much smaller when condensation occurs. This indicates that the densities of saturated vapor and liquid are approaching each other. It is also evident that the properties of CO_2 liquid and vapor are becoming similar and will eventually coincide. This in fact is realized at 31.1°C Isothermal, which does not show horizontal discontinuity. We therefore have continuity of states.

Figure 2.16 is a typical way to use critical point drying to avoid surface tension induced damages. The sample is immersed in the liquid CO_2 at the phase equilibrium of the vapor phase. The temperature is raised beyond critical temperature, and held there while the pressure is decreased by venting the CO_2 slowly. The sample is then dried without experiencing any abrupt phase transition or surface tension. In the CPD procedure, the initial status also makes differences, as shown in Figure 2.16. If the start point is X, where liquid has more volume than vapor (or more than half of the chamber is filled with liquid), the pressure of the system may be too high when it reaches the critical point, and the pressure relief valve is used to decrease the pressure. On the other hand, if the start point is Z, where less than half of the chamber is filled with liquid, the liquid may start to vaporize before reaching the critical point when the temperature is raised. This may leave the sample uncovered with liquid. Therefore, a proper start condition should be used for a good drying.
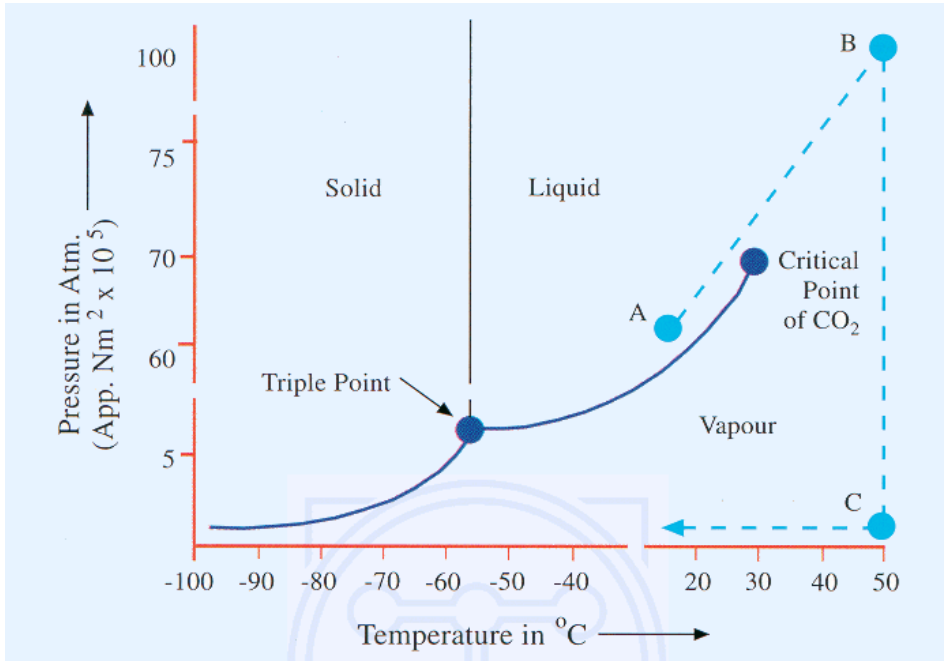
Figure 2.15 Phase diagram of CO_2 and typical CPD route [38]
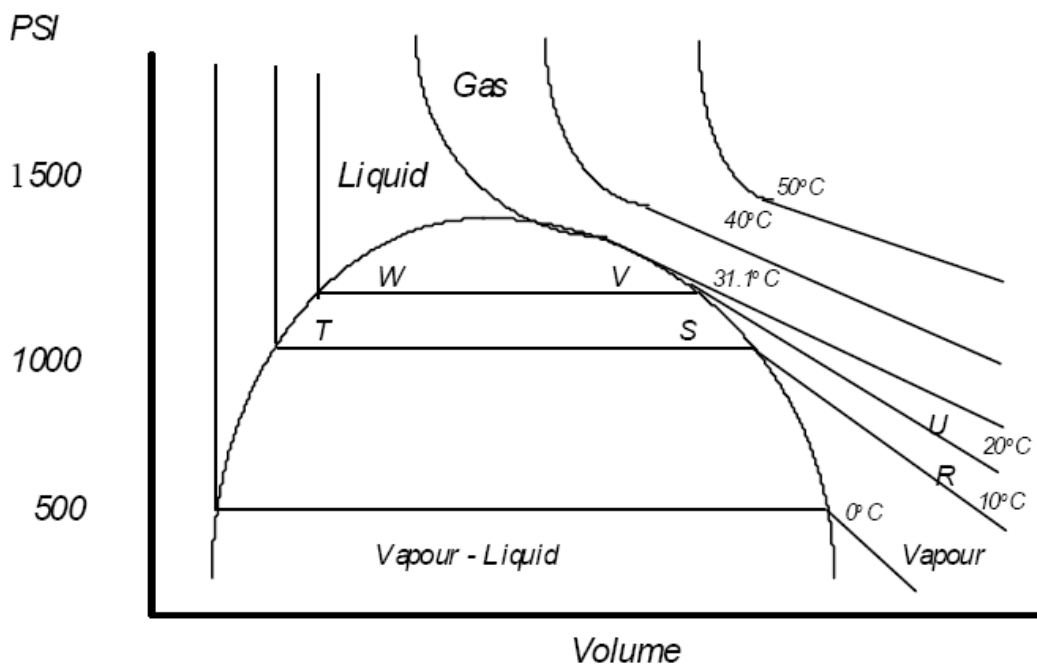
Figure 2.16 Pressure-Volume relation of CO_2 at different temperature

35
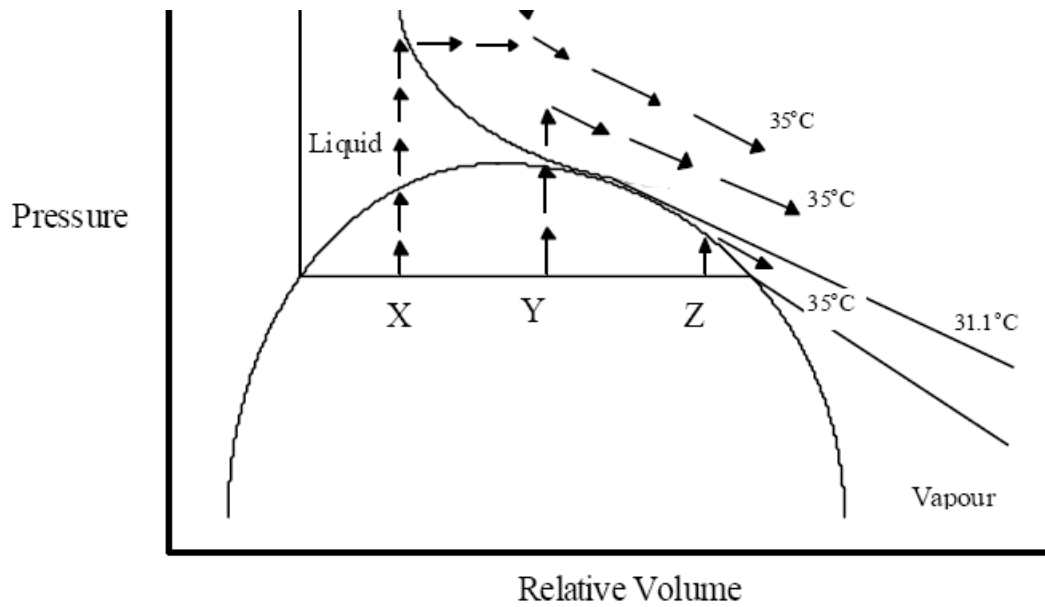
Figure 2.17 Condition changes during critical point drying

Intermediate/Dehydration Liquid

Because the CO_2 is not miscible with water, some intermediate liquid should be used to replace the water. This step is critical because the CPD result is directly related to the completeness of the water replacement and dehydration. Table 2.3 shows three intermediate fluid candidates. Acetone and Ethanol are chosen based on environmental consideration.

DEHYDRATION/INTERMEDIATE FLUIDS FOR C.P.D.	
SUBSTANCE	SURFACE TENSION (DYNES/CM)
ETHANOL	23
ACETONE	24
FREON (113)	19

Table 2.3

CPD set up

Figure 2.18 illustrates the set up of the CPD process. A Siphon cylinder provides the liquid CO_2 source to the Quorumtech E3100 critical point dryer. The temperature of the chamber is controlled by a Quorumtech E4800 circulating heater and chiller. Internal pressure can be manually controlled by adjusting the valves of the liquid CO_2 drain and vapor CO_2 vent. The liquid surface can be monitored by the flow rate of the CO_2 drain and input.
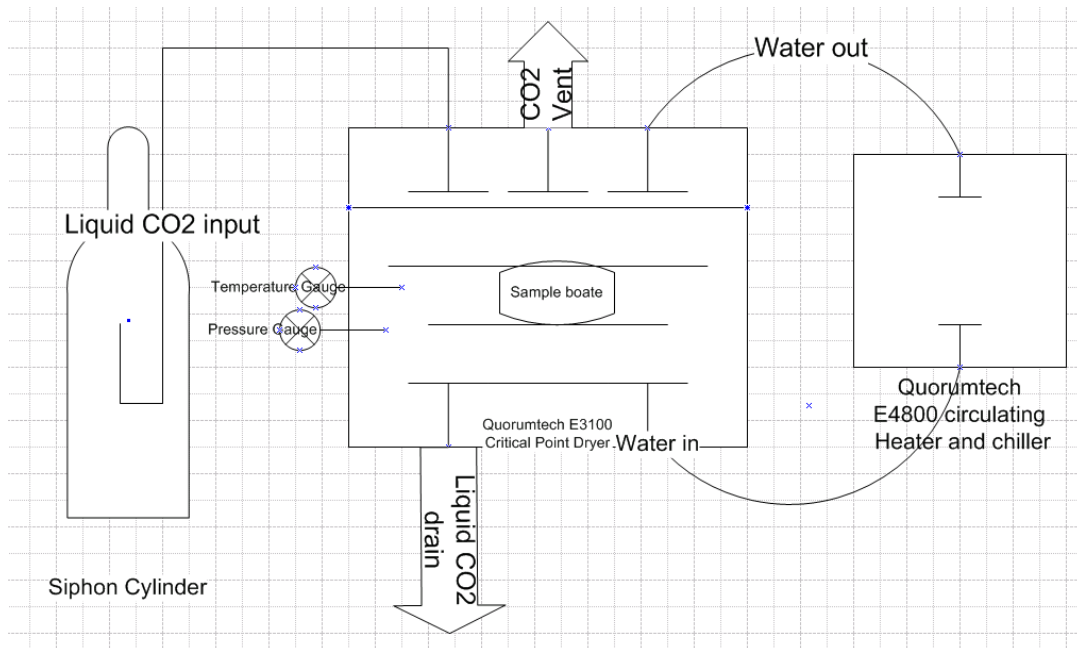
Figure 2.18 CPD experiment set up

CPD Process flow

Figure 2.19 shows the flow chart of CPD process. After the sample is etched by wet chemicals, it is rinsed with water. The water is then replaced with Acetone by mixing it with Acetone and pouring out part of it again and again. Better equipment should provide a dynamic flush and drain of Acetone. In this process, the complete replacement of water is ensued by doing multiple processes and Acetone soaking. The sample is then transferred to a boat and loaded into the chamber. The chamber should be chilled at 5°C. After the loading, the sample is flushed with liquid CO_2 for 5 minutes, followed by a 10-minute soak. The flush and soak are repeated twice to ensure that the Acetone is totally gone. Liquid CO_2 is kept at an optimum height as discussed previously and all of the valves are closed. The temperature is raised to ~40°C, while the pressure is increased

38

to ~1200 PSI simultaneously. During this process, the disappearance of the vapor-liquid interface can be observed, which is a good indication of the CO_2 passing the critical point. After passing the critical point, the pressure can be decreased by gradually opening the venting valve. This venting process must be very slow to prevent the CO_2 from re-condensing. It takes ~40-60 minutes for the venting process. The chamber can then be opened to unload the sample boat, after the pressure returns to atmosphere.
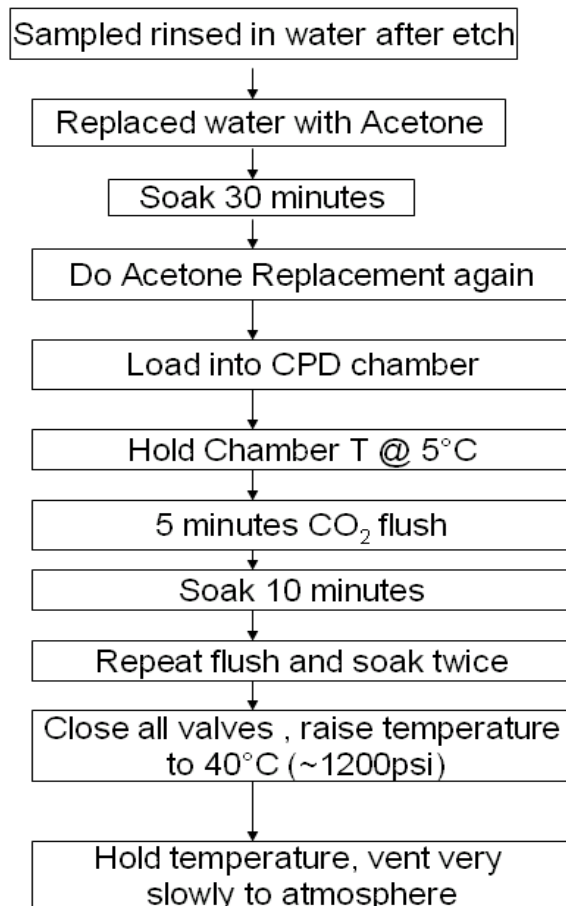

Figure 2.19 CPD process flow

2.4.1.3 Crystallographic Etching

Selectivity

Selective etching of sacrificial layers by undercutting using a wet etchant is a critical step for suspended structure fabrication. For VCSEL DBRs, the thickness accuracy and surface quality are crucial. It greatly affects the reflectivity and optical loss. Therefore, the layers to be grown, their composition and thickness, the selective etchant, the pattern dimensions and the masking technique must be optimized.

In this work, GaAs/AlGaAs is chosen because it is a mature DBR combination for GaAs substrates. Wet etchants for AlGaAs with high selectivity to GaAs are available. Diluted HCl, diluted HF or diluted buffered oxide etch have effectively infinite selectivity to etch AlGaAs from GaAs[39]. HF based etchant tends to degrade the adhesion between photoresist and the sample surface during long etchings. However, the etch rate must be slowed down in order to achieve clean surface, which requires an alternative masking technique other than the commonly used photoresist. HCl is a better solution in this perspective. The etching can be well controlled, and it is very mild to normal photoresist. After calibrating various AlGaAs and HCl etchant compositions, $Al_{80}Ga_{20}As$ and HCl/water (1:1) are chosen. This gives a very well controlled etching rate of $\sim$ 0.8-1μm/minute and a very nice, clean GaAs face after etching. The photoresist (AZ5214) remains intact after a typical 12~15 minute etching.

Anisotropy

Wet chemical etching, like any chemical reaction, exhibits two different modes. One mode is reaction-rate limited etching and, the other is mass-transfer-rate limited etching. In our experiments, we observed both depending on the etch window size. When the window dimension is smaller than 4μm, it generally shows a mass-transfer-rate limited etching mode. The undercut area extends uniformly in all directions. The etching mode transits to reaction-rate limited when the window size is bigger than 5μm and the undercut pattern will depend on the different etching rate for different crystalline planes. III-V compound semiconductors with zinc blend symmetry usually follow the etching rate sequence: {110}>V-{111}>{100}>III-{111} for low index planes.

In this work, $Al_{80}Ga_{20}As$ exhibits similar behaviors, as shown in Figure 2.20. Two squares are etch-window prepared using reactive ion etching (RIE). The picture was taken with infrared CCD camera for longer penetration depth. It clearly shows that the {110} planes have the fastest etching rate. By aligning the etch-window with the correct direction, the AlGaAs underneath can be etched away in this preferred manner, as shown in Figure 2.20, where minimum AlGaAs material is removed. In this way, more AlGaAs material is left to provide mechanical supports and the paths for electrical and thermal conduction. A very gentle stirring is usually applied while etching to help keep the etching in the reaction-rate limited mode.
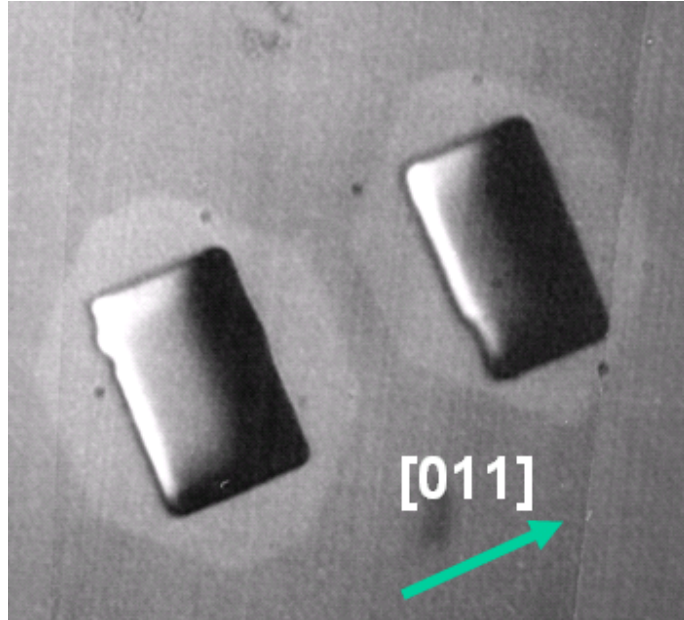
Figure 2.20 crystallographic underetching of $Al_{80}Ga_{20}As$ with HCl/water(1:1) for 7 minutes at room temperature. Very gentle stirring applied.
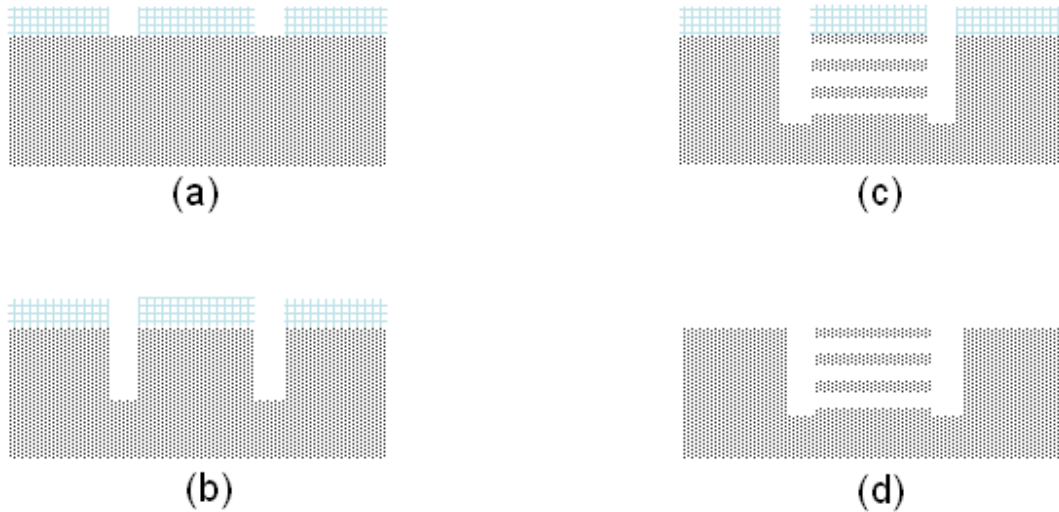
2.4.1.4 Process Flow

Figure 2.21 Process flow of type I air-gap DBR. (a) Etch-window defined by lithography; (b) Etch-window etched by RIE; (c) $Al_{80}Ga_{20}As$ etched by HCl/water (1:1) undercut; (d) Rinse and dry with (water->Acetone->CPD)

A process flow is developed based on selectively etching away $Al_{80}Ga_{20}As$ sacrificial layers and releasing them with critical point drying (CPD). Multiple $GaAs/Al_{80}Ga_{20}As$ pairs are grown via molecular beam epitaxy (MBE). The process flow illustrated in Figure 2.21 is carried out. Two rectangular etch-windows (20μm by 30μm) are defined by common lithography using photoresist AZ5214. The windows are etched using RIE with $SiCl_4$ and BCl_3 chemistry. Thus the sidewalls of the $Al_{80}Ga_{20}As$ layers are exposed for undercut. The sample is then put into $HCl:H_2O$ (1:1) etchant for 10-15 minutes depending on the mirror size. After the mirrors are etched through, the sample is rinsed and loaded into the critical point dryer to finish the drying and release process.

Figure 2.22 is a bridge structure fabricated by this technique. It is a one λ cavity sandwiched by 3 pairs of GaAs/air-gap top DBRs and 4 pairs of GaAs/air-gap bottom DBRs. The SEM picture shows the seven air-gaps hold very well. There is no distortion or stiction found in the picture. Figure 2.23 is a closer side-view of this 7-layer structure, which shows that the suspended GaAs layers stay very flat. The dark strips are the side-view of the etched air-gaps and the light areas indicate GaAs layers. Figure 2.24 is the top-view picture taken by infrared CCD camera. The shadow region in the center is the under cut area, which shows that the air-gaps have been etched through, and they are flat, indicated by the uniform grey scale. The crystallographic etching is also evident from the picture. Figure 2.25 shows a similar structure with some of the layers distorted or adhered together. The reason for this failure is that the CO_2 and soak was not done correctly. Some Acetone, or even water, is trapped between the GaAs layers. When they are vaporized, the surface tension pulls them together, as discussed before.

In summary, by using the right design of structure and geometry, and optimizing the etching and CPD techniques, the development of a high yield and robust processing technique for air-gap DBRs is accomplished.
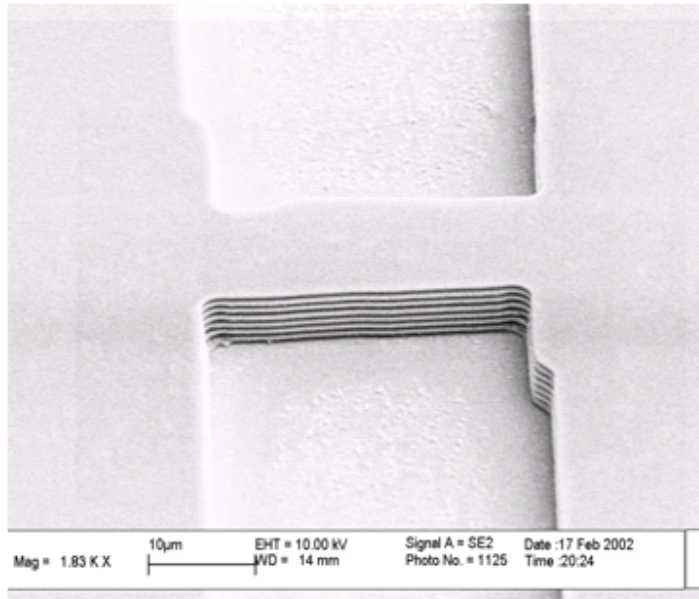
Figure 2.22 7 pairs of GaAs/air DBR structure
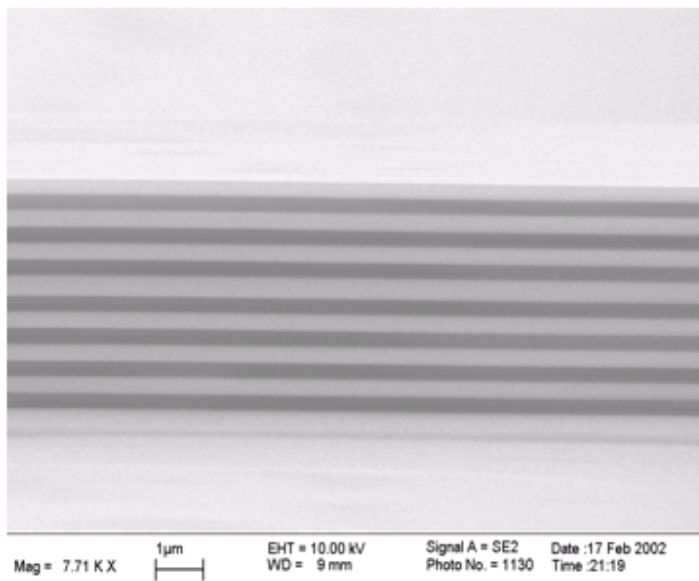
Figure 2.23 closer side-view of 7-pair DBR structure
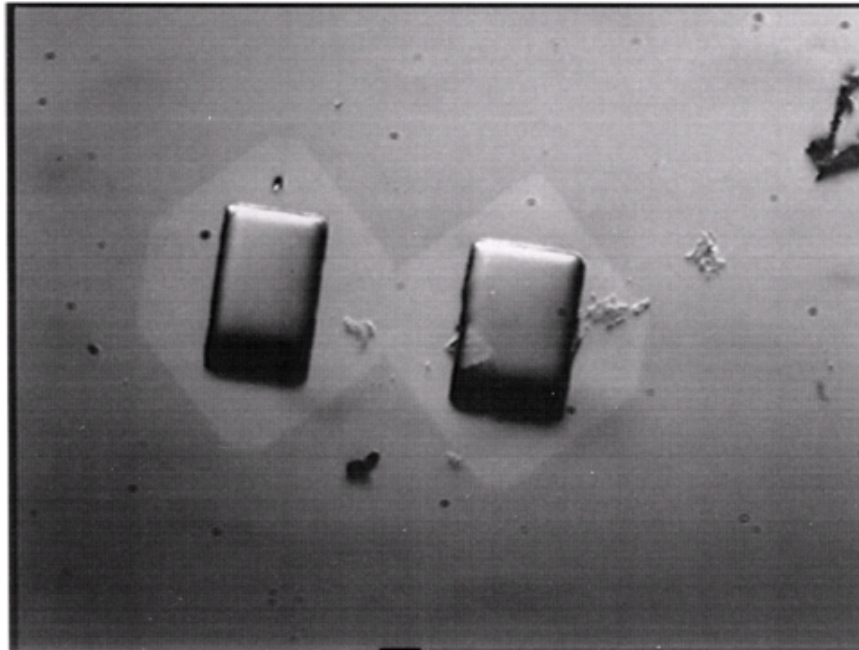
Figure 2.24 Top view of a 7-layer DBR shows uniform undercut shadow and crystallographic etching
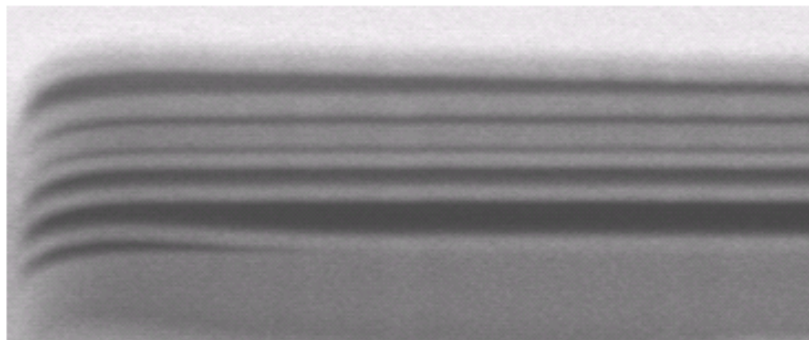
Figure 2.25 side-view of a 7-layer DBR after improper rinse and drying

2.4.2 Type II Hybrid Air-gap DBR development
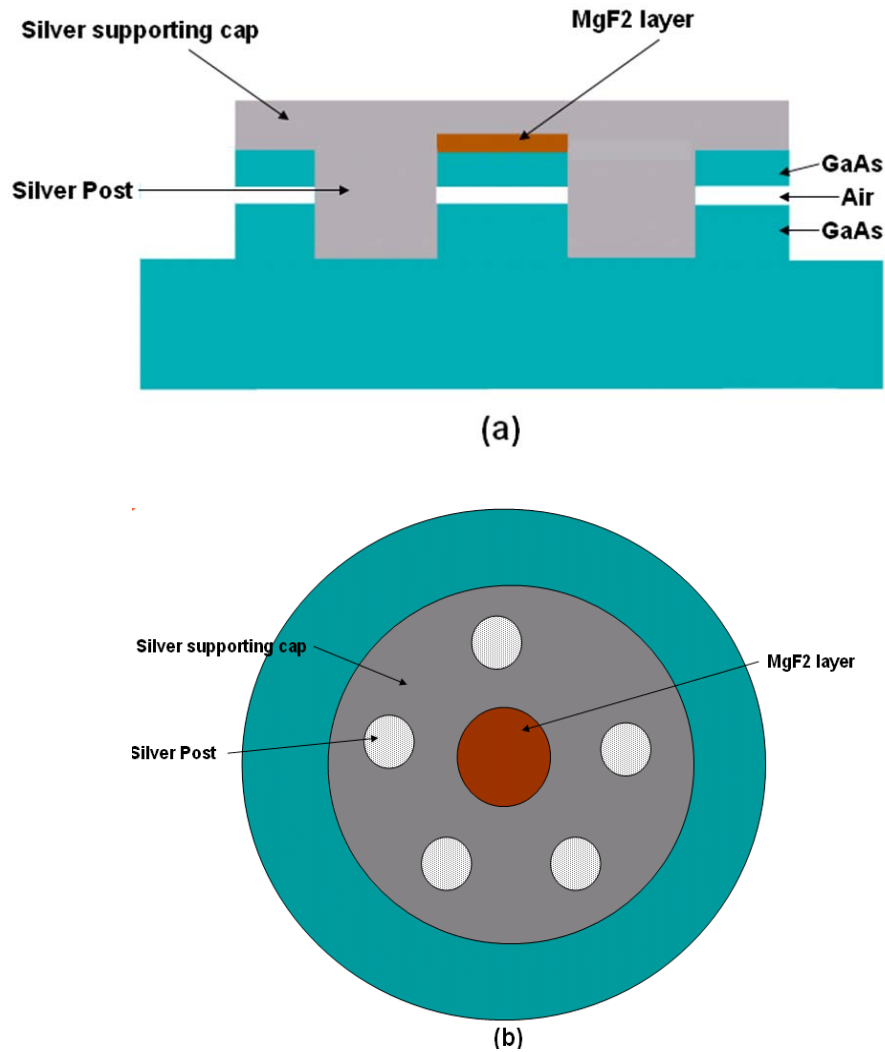
Figure 2.26 schematics of type II hybrid air-gap DBR
(a) side view, (b) top view

As proposed in chapter 2.3, a hybrid air-gap DBR combining a metal reflector, air-gap and dielectric mirror can present a very high reflectivity and wide bandwidth. It is also a robust structure and process, because there is only one air-gap included in the

structure. The drawback is that this structure is only good for one side of the cavity because of the opacity of the metal reflector.

The approach taken in this project is shown in Figure 2.26. The free-standing structure is held by a silver cap and 5 silver posts. The silver post is 5μm in diameter and the silver cap is 2μm in thickness. The silver posts are standing on the GaAs layer under the air-gap and the silver cap is adhered to both the silver posts and the GaAs layer on top of the air-gap. Such a structure is mechanically very stable with straightforward processing. Also the silver posts and cap can improve the thermal dissipation of the device, which is crucial for air-gap VCSELs.

2.4.2.1 Process Flow

The process flow for type II hybrid air-gap DBRs is illustrated in Figure 2.27. After the wafer is grown with MBE, a MgF_2 film is deposited with a Leybold E-beam deposition system after lithography patterning of the photoresist. A MgF_2 disk with a 15μm diameter is defined by the photoresist lift-off technique. Five holes with 5μm diameter are defined by photolithography and RIE etch. The depth of these holes is enough to etch through $Al_{80}Ga_{20}As$ sacrificial layer into the GaAs layer underneath. This provides a solid ground for silver supporting posts to stand on. The photoresist is not striped off after RIE because it is necessary for lift-off in the next step. The sample is then loaded into a CHA E-beam deposition system. Silver film is deposited to fill these holes. Lift-off is carried out to

remove all of the silver on the surface, and only the silver inside the holes remains. This leaves a flat surface for the silver cap layer. The sample is loaded into the CHA E-beam deposition system again, and a 2μm silver film is coated on top of the wafer. This is followed by photolithography and wet chemical etching to define the silver disk. Commercially available TRANSCENE silver thin film etchant is used in this step. An isotropic wet etching (H_2SO_4:H_2O_2:H_2O = 1:8:80) is performed afterwards to etch through the top GaAs layer and the $Al_{80}Ga_{20}As$ sacrificial layer. Now the side-wall of the sacrificial layer is exposed and a wet selective etching is done to undercut and eventually remove the entire sacrificial layer. This completes the process.

Figure 2.28 shows the process results of a type II DBR structure. As the SEM pictures indicate, the sacrificial layer has been removed. The silver disk and GaAs layer attached to it from underneath are supported by five silver posts. No collapse is found across the wafer, which indicates a good yield. Of course, SEM is not an effective technique for determining the status at the center of the mirror, thus the emission spectra of electroluminescence or photoluminescence is used, as discussed in next section.
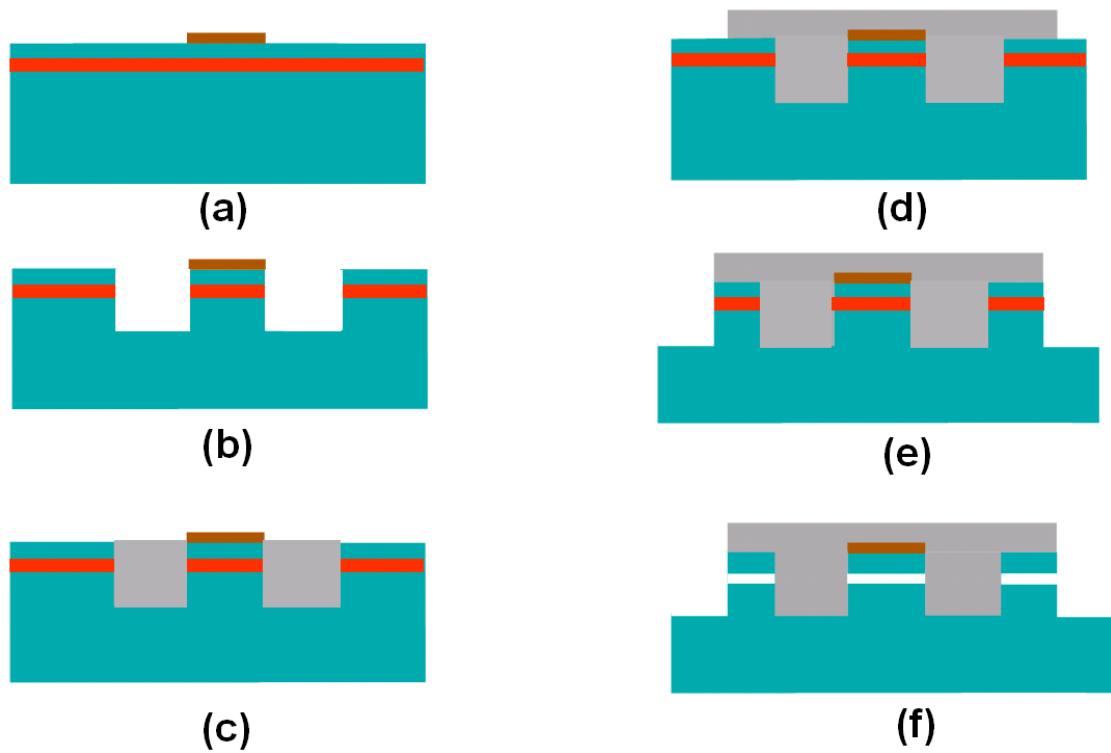
Figure 2.27 Type II hybrid air-gap DBR process flow (a) MgF$_2$ mirror defined by lift-off after E-beam deposition. (b) Five holes etched by RIE. (c) Five-holes are filled with silver by E-beam deposition. (d) Silver cap defined by lift-off after E-beam deposition. (e) Mesa etched by wet etching. (f) Sacrificial layer removed by wet etching undercut

(a)
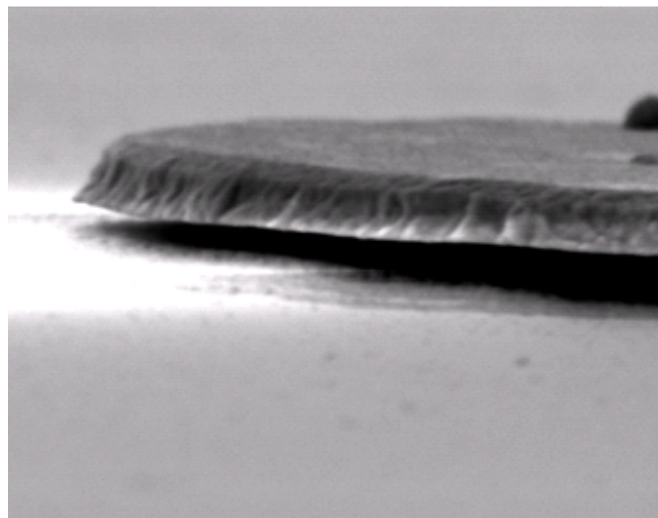
(b)

Figure 2.28 (a) Overview of a type II hybrid DBR structure
(b) A closer side-view of the suspended silver disk supported
by five silver posts

.

2.4.3 Air-gap DBR Characterization
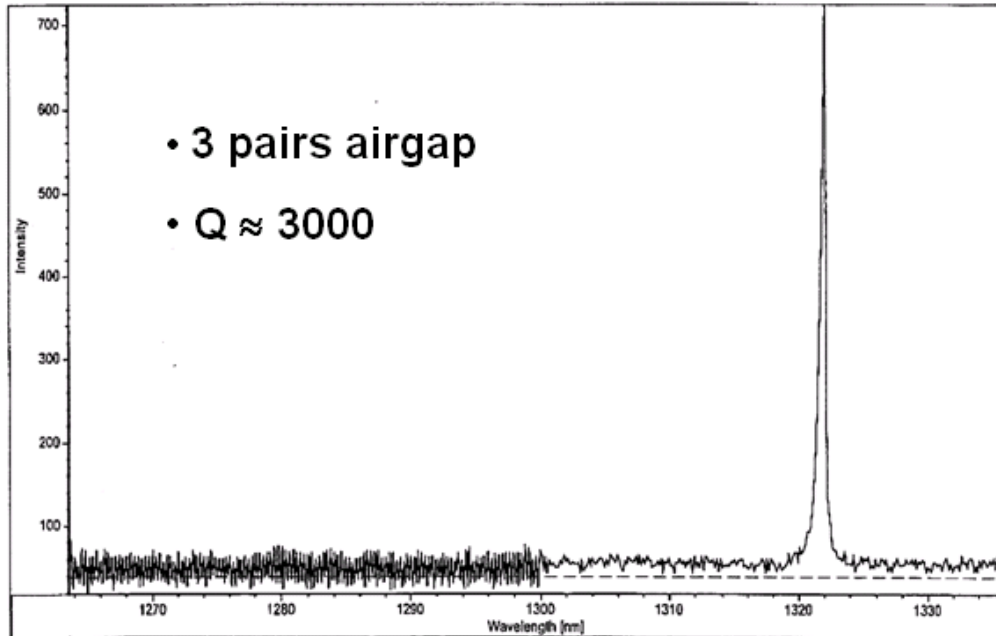
Figure 2.29   Micro-photoluminescence from a one-λ cavity with 3-pair GaAs/air as top DBRs and 25 pairs of GaAs/AlAs as bottom DBR. InAs quantum dots emitting at 1.3μm are used as the active region.

Before the developed air-gap is integrated into the VCSEL, some preliminary characterizations are performed to examine the performance of these novel mirrors. A one-λ microcavity sample is grown with MBE. The top DBR is formed by 3 pairs of GaAs/air mirror and the bottom mirror consisted of 25 pairs of GaAs/AlAs semiconductor mirrors. One sheet of InAs quantum dots is used as an active region embedded in the center of the cavity. Micro-photoluminescence is done by focusing the pumping laser source using an objective onto the center of the air-gap DBR and collecting the excited

52

photoluminescence signal. The emission spectrum shown in Figure 2.29 has a FWHM of 4Å, which indicates that a microcavity with a quality factor Q~3000 is formed. Although the Q factor is much lower than the theoretical value (>20000), it clearly shows that the air-gaps are successfully formed and start working, although the quality still needs improvement.

An electrically pumped microcavity was also built to preliminarily characterize the quality of air-gap DBRs. To simplify the processing, a single pair of GaAs/air-gap mirror is incorporated. The schematic of this structure is shown in Figure 2.30. It is a one-λ cavity with InAs quantum dots embedded in the center as an active region. The quantum dots are emitting at 1.3μm. The bottom mirror is formed by 31 pairs of N-doped GaAs/AlAs semiconductor DBRs. Lateral current and optical confinement is provided by AlO_x aperture converted from AlGaAs by thermal oxidation. This confinement is very important for efficient VCSEL operation. Figure 2.31 shows the electroluminescence spectrum when current is injected into the device. The measured quality factor (~250) is well matched with the transmission matrix modeling. This match shows the air-gap is working properly as designed. However, the yield of the process used in this scheme is low, which we attribute to the strain and volume shrinkage induced by wet oxidation of the AlGaAs layer[40]. This raises a serious processing integration problem for air-gap DBR based VCSEL devices. This problem and its solution will be discussed in more detail in next chapter.
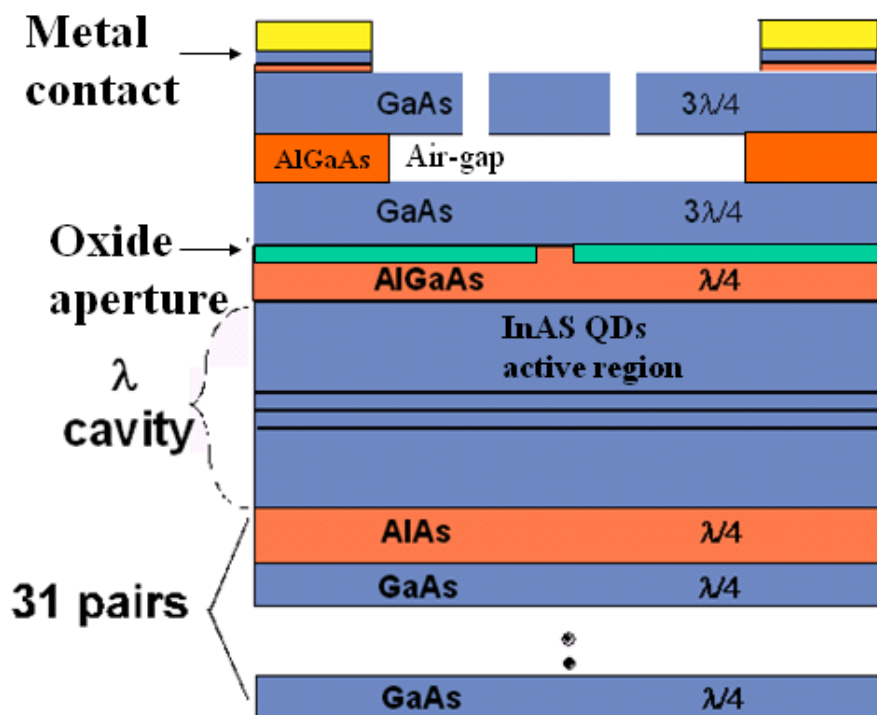
Figure 2.30　Electrically pumped microcavity formed with one air-gap DBR on the top and 31 pair of GaAs/AlAs at the bottom. Lateral optical and current confinement is realized by native oxide aperture converted from AlGaAs by wet thermal oxidation.
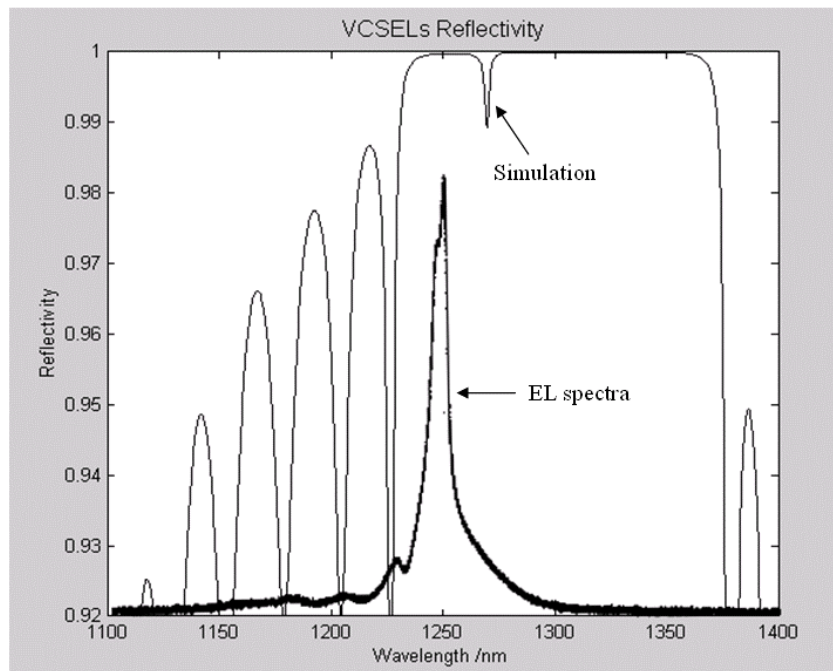
Figure 2.31 Electroluminescence of one-pair air-gap DBR structure, the FWHM (Q factor) matched that of the simulated spectrum

2.5 Summary

Distributed Bragg reflectors are an essential component to provide the high reflectivity necessary for VCSEL lasing operation. However, the absence of a suitable DBR is usually a major hurdle for VCSEL development.

The air-gap DBR is a potential solution to this problem. The large refractive index contrast and good interface quality enable high reflectivity with a very small number of pairs. The analysis shows its advantages also include a wide stop-band and shorter penetration depth. The air-gap DBR can be made from any pair of materials, given that a highly selective etching is available between them. This flexibility eases many of the

material compatibility issues often emerging during VCSEL development.

Two types of air-gap DBR are proposed. One contains multiple semiconductor/air-gap stacks, and the other is a hybrid structure combining air-gap, dielectric and metal reflectors.

Processes for both types of DBRs were developed. The fundamental issue in air-gap mirror fabrication is the stiction problem, which is induced by the surface tension of diminutive liquid when the devices are exposed for rinse and drying. Critical point drying and silver supporting posts are used in type I and II structures, respectively, to counteract this problem. Both types are successfully demonstrated. SEM, electroluminescence and photoluminescence are used to confirm that these mirrors are functioning. The exhibited characteristics are matched well with the transmission matrix simulation.

Chapter 3

Air-Gap VCSEL: Process Integration and Device Demonstration

3.1 All-epitexial Current and Optical Confinement Technique

3.1.1 Introduction

Efficiently pumping a small volume gain region in a low loss (high Q) semiconductor cavity is crucial for VCSEL operation. The optical loss includes vertical and lateral components. The vertical loss is mostly due to the non-unity mirror reflectivity, which can be controlled and improved by high reflectivity and high contrast DBRs. The lateral loss is ultimately due to diffraction and comparatively small to the vertical loss, until the lateral mode size reaches a certain minimum value determined by vertical loss rate[41]. The Q starts decreasing significantly once the mode size is smaller than this minimum for a planar cavity. By introducing a thin dielectric aperture into a high Q cavity, this limitation is greatly reduced[42]. This discovery is a milestone toward efficient high-performance VCSEL development and was adopted by the industry as a standard technology. The current standard method is performed by wet thermal oxidation to convert part of the Al(Ga)As layer into AlOx. However, the volume of the AlOx tends to be reduced compared to that of

the original semiconductor layer, due to the small volume of O ($\sim 2.85 \text{Å}^3$) compared to Al ($\sim 3.57 \text{ Å}^3$). This translates to a theoretical volume shrinkage of 20% and is measured experimentally at 13%. The huge thermal strain and uneven surface resulting from this shrinkage are the main culprits responsible for the low yield of air-gap DBR. The Changes in etch behavior of $Al_{80}Ga_{20}As$ and GaAs after this wet thermal cycle are another factor, which deserves more careful study.

A new integration process flow was developed based on a novel all-epitaxial confinement technique. This technique provides a nice base for building air-gap DBRs, in addition to many other advantages. This chapter starts with an explanation of lateral diffraction loss in a planar cavity and a model of effective lateral loss suppression. The all-epitaxial confinement technology will be discussed, followed by a description of the process integration of air-gap DBRs. Working air-gap DBR based VCSELs are demonstrated. The experimental data is presented and analyzed at the end of this chapter.

3.1.2 Lateral Diffraction Loss

A simplified model of a point source radiating from inside of a planar Fabry-Perot cavity is illustrated in Figure 3.1[43]. The cavity is formed by two reflectors with reflectivity and transmittance of ρ_1, τ_1, ρ_2, and τ_2, respectively. The E-field starts as E_{in} and the transmitted field amplitude is built up each time the traveling wave hits the mirror. As shown in Figure 3.1, both the radiance with θ and $(180 - \theta)$ contribute to the field in same

direction. The output field E$_{out}$ can be calculated as the sum of all of the fields:

$$E_{out} = E_{out}(\theta) + E_{out}(180 - \theta)$$
$$= E_{in}\tau_2 \exp(\phi) + E_{in}\rho_2\rho_1\tau_2 \exp(\phi + ik\Lambda) + \cdots \qquad \text{Equation 3.1}$$
$$= E_{in}\rho_1\tau_2 \exp(\varphi) + E_{in}\rho_1^2\rho_2\tau_2 \exp(\varphi + ik\Lambda) + \cdots$$

where Λ is the optical path difference after each round trip, which is determine by the

cavity length L and radiation angle θ as in Equation 3.2:

$$\Lambda = 2L\cos\theta \qquad\qquad \text{Equation 3.2}$$

ϕ and φ are the arbitrary starting phases for E$_{out}(\theta)$ and E$_{out}(180 - \theta)$. They are related to

each other by Equation 3.3:

$$\varphi = \phi + iK\Lambda/2 \qquad\qquad \text{Equation 3.3}$$
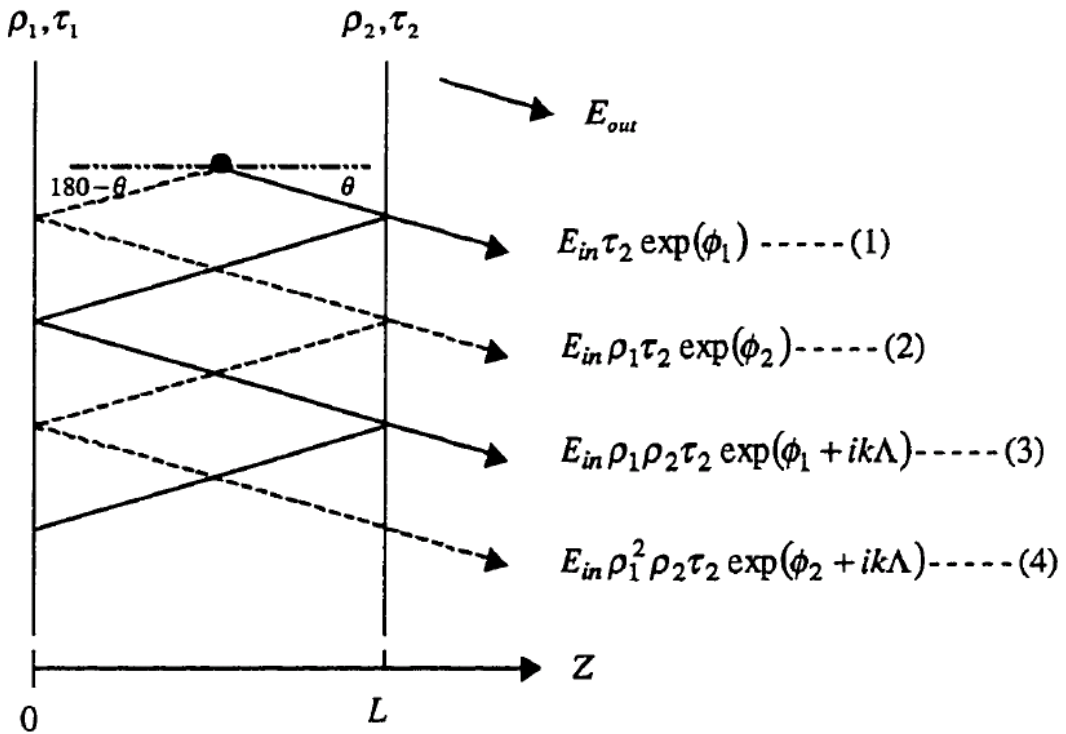
Figure 3.1   Model for diffraction loss of a point source
embedded in a planar Fabry-Perot cavity.

The intensity ratio of transmitted field to the original field can be found as:

$$\left|\frac{E_{in}}{E_{out}}\right|^2 = \frac{(1-R_2)(1+R_1+2\sqrt{R_1}\cos(KL\cos(\theta)))}{\left(1-\sqrt{R_1R_2}\right)^2+4\sqrt{R_1R_2}\sin^2(KL(\cos\theta))} \qquad \text{Equation 3.4}$$

R and R_2 are equal to $\rho_1{}^2$ and $\rho_2{}^2$, respectively. The angular dependence of this intensity ratio is evident and leads to a decrease of transmitted light when θ increases. This implies the existence of an exit cone with a certain solid angle. When the divergence of this radiant source is bigger than this exit cone, part of the light will bounce back and forth between the mirrors and eventually be lost in the lateral direction. With small angle approximation, the FWHW angle θ_0 can be expressed as:

$$\theta_0 \approx \sqrt{\frac{(1-R)\lambda}{2\pi L}} \qquad \text{Equation 3.5}$$

With the Gaussian beam approximation, this divergence angle can be translated to an equivalent mode size as:

$$W_0 = \sqrt{\frac{\lambda L}{\pi(1-R)}} \qquad \text{Equation 3.6}$$

This is the minimum mode size set by the planar Fabry-Perot cavity. When the mode size is below this number, diffraction loss arises and part of the emission will be cut off. To achieve efficient lasing in small mode volume, effective optical confinement must be applied to the microcavity to suppress the lateral diffraction loss.

3.1.3 Suppression of Lateral Diffraction Loss

A strategically placed intracavity dielectric aperture, either an etched void[44] or a native oxide,[42] can effectively confine the optical mode and suppress lateral diffraction loss. A simple model can be used to explain this strong confinement[45]. This model also provides a theoretical base for the development for all-epitexial confinement technique, which will be discussed in the next section and is critical for the success of the process integration in this work.
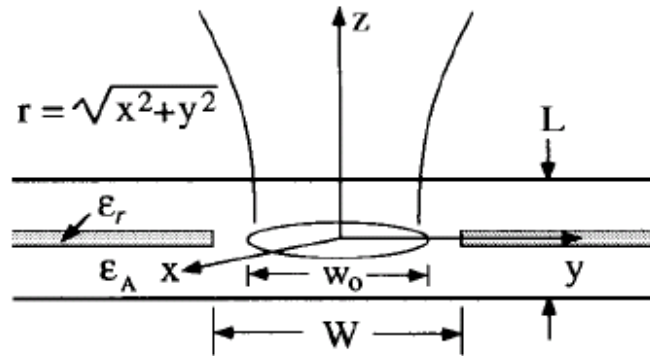
Figure 3.2   Schematic of a Fabry-Perot microcavity with dielectric aperture and coordinate system used in the model.

The microcavity with a dielectric aperture can be simplified as illustrated in Figure 3.2. Considering an ideal Fabry-Perot microcavity with unity mirror reflectivity, we can define two regions. Region $r < W$, confined by the aperture, has a dielectric constant $\varepsilon = \varepsilon_A \varepsilon_0$, where ε_0 is the free space dielectric constant and has a cylindrical symmetry. Region

61

$r \geq W$ is the cladding region, which contains a dielectric layer, with dielectric constant $\varepsilon_r <$ ε_A, and extends laterally outward to infinity in x-y plane. To further simplify this model, the cladding region is treated as having an average dielectric constant $\varepsilon = \varepsilon_{WG}\varepsilon_0$, with $\varepsilon_{WG} < \varepsilon_A$. The physics picture of this model can be perceived as an oscillating eigenmode acting like a radiation source confined in three dimensions, whose only chance for lateral escape is to excite or couple into the parasitic waveguide modes in the cladding region. We assume perfect vertical mirrors here; therefore, the mode is confined without loss in the vertical direction. This chance to travel laterally is determined by the mode density excited in the cladding region and a spatial overlap integral for each individual parasitic mode. The dependence of the mode density on frequency can be derived in a classical way. The total number of optical modes in any cavity can always be counted as:

$$\# \, Modes = \sum_{s=1}^{2} \sum_{m_x=-\infty}^{\infty} \sum_{m_y=-\infty}^{\infty} \sum_{m_z=-\infty}^{\infty} \qquad \text{Equation 3.7}$$

S denotes two different polarizations. m_x, m_y and m_z are determined by the boundary condition of resonance:

$$2k_i L_i = 2m_i \pi \qquad (i = x, y, z) \qquad \text{Equation 3.8}$$

L_x, L_y and L_z are the dimensions of an optical cavity. $\left| \vec{K} \right| = \omega n/c = \sqrt{k_x^2 + k_y^2 + k_z^2}$, where ω is the resonant frequency and c is the speed of light. Since the cladding region is assumed to extend laterally to infinity in the x-y plane, the summation over m_x and m_y can by replaced by an integral as:

62

$$\# Modes = \sum_{s=1}^{2} \sum_{m_z=0}^{\infty} \frac{L_x L_y}{\pi^2} \int_{-\infty}^{\infty} dk_x \int_{-\infty}^{\infty} dk_y$$

$$= \sum_{s=1}^{2} \sum_{m_z=0}^{\infty} \frac{L_x L_y}{4\pi^2} \int_{0}^{2\pi} d\varphi \int_{0}^{\infty} k_\rho dk_\rho \qquad \text{Equation 3.9}$$

$$= \sum_{s=1}^{2} \sum_{m_z=0}^{\infty} \frac{L_x L_y \varepsilon_{WG}}{2\pi c^2} \int_{\frac{\pi m_z}{L_z}}^{\infty} \omega d\omega$$

Therefore, the mode density in the cladding region has a frequency dependence as a slanted staircase shown by the solid curve in Figure 3.3. Each step occurs at the frequency of $\dfrac{\omega}{c} = \dfrac{\pi m_z}{\left(\sqrt{\varepsilon_r} L_z\right)}$. On the other hand, the confined aperture region has discrete allowed frequency due to the confined eigenmodes, which is shown as a sharp resonance peak in Figure 3.3.
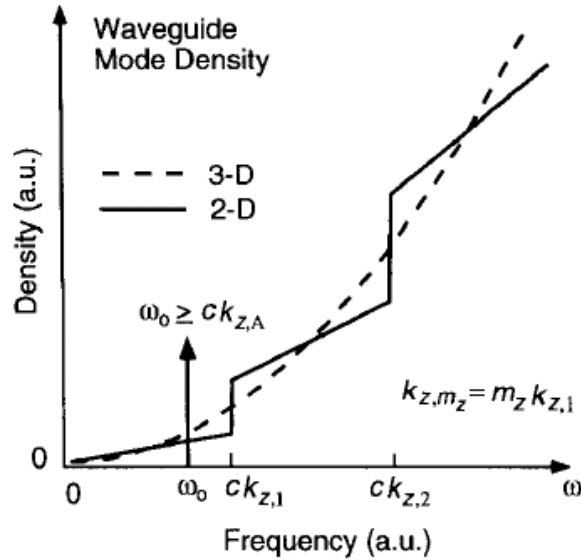

Figure 3.3 Optical density vs. frequency in the 2-D cladding region. Dashed curve are 3-D case with no confinement for comparison.

63

In order to excite the parasitic modes in the cladding region, the resonant frequency of the eigenmode ω_0 in the confined aperture region must be the same as in the cladding waveguide region:

$$\frac{\omega_0}{c} = \sqrt{\frac{(4.810)^2}{\varepsilon_A w_0^2} + k_{z,A}^2} = \sqrt{k_{\rho,WG}^2 + k_{z,WG}^2} \qquad \text{Equation 3.10}$$

$$k_{z,A} = \frac{\pi m_z}{\sqrt{\varepsilon_A} L_z}, \quad k_{z,WG} = \frac{\pi m_z}{\sqrt{\varepsilon_{WG}} L_z} \qquad \text{Equation 3.11}$$

The factor of 4.810 comes from the cylindrical symmetry and assumption of a Bessel function solution for the field in the aperture[46]. The optical mode size is characterized by w_0. From Equation 3.10, we can derive:

$$k_{\rho,WG} = \sqrt{\left(k_{z,A}^2 - k_{z,WG}^2\right) + \frac{(4.810)^2}{\varepsilon_A w_0^2}} \qquad \text{Equation 3.12}$$

Since the cladding waveguide region has a smaller average dielectric constant, it leads to $k_{z,A} < k_{z,WG}$ according to Equation 3.11. Thus there exists a range of w_0 resulting in a minus number under the square root in Equation 3.12. In this circumstance, $k_{\rho,WG}$ is an imaginary number which indicates an evanescent field in the cladding waveguide region. In other word, this eigenmode is confined inside the aperture. This minimum mode size is defined by Equation 3.12:

$$w_0 \geq \frac{4.810}{\sqrt{\varepsilon_A \left(k_{z,WG}^2 - k_{z,A}^2\right)}} \qquad \text{Equation 3.13}$$

This confinement mechanism results from the important inequality $k_{z,A} < k_{z,WG}$,

64

which indicates a vertical resonance blue shift of the cladding region from the aperture region. Two critical points can be derived from this fact. First, this inequity originates from the resonant condition of Fabry-Perot cavity. Therefore the resulting confinement is not due to the aperture alone, but due to both the aperture and the Fabry-Perot cavity. Second, the key to achieve this confinement is the blue shift of the vertical resonance set by the cladding layer. It does not matter by what means this blue shift is realized. According to 3.11, it is evident that in addition to a lower refractive index material in the cladding layer, shortening the effective cavity length or forcing the cladding layer to resonate at a higher order mode can also attain this blue shift. The latter two methods provide the theoretical base for the all-epitaxial confinement, which is used in this work and will be discussed in more detail in the next section.

Figure 3.4 is a typical reflectivity spectrum of a VCSEL with an oxide aperture. As expected, the cladding region (b) shows a blue shift in the vertical resonant wavelength compared to that of the aperture region (a). According to Equation 3.13, the greater the blue shift, the smaller the optical mode can be achieved without suffering serious lateral optical loss. The optical confinement mechanism is also confirmed by Hadley's effective index model[47]:

$$\frac{\Delta n_{eff}}{n_{eff}} \approx \frac{\Delta \lambda_0}{\lambda_0} \qquad \text{Equation 3.14}$$

where n_{eff} and λ_0 are the effective index and vertical resonant wavelength, respectively.

This reveals that the blue shift is equivalent to a low effective index, which results in the optical waveguide effect. Again, there are many approaches for achieving this blue shift, which leaves more flexibility in the device design.

In the next section, an alternative all-epitaxial technique will be discussed as an alternative to the native oxide aperture for lateral optical and current confinement.
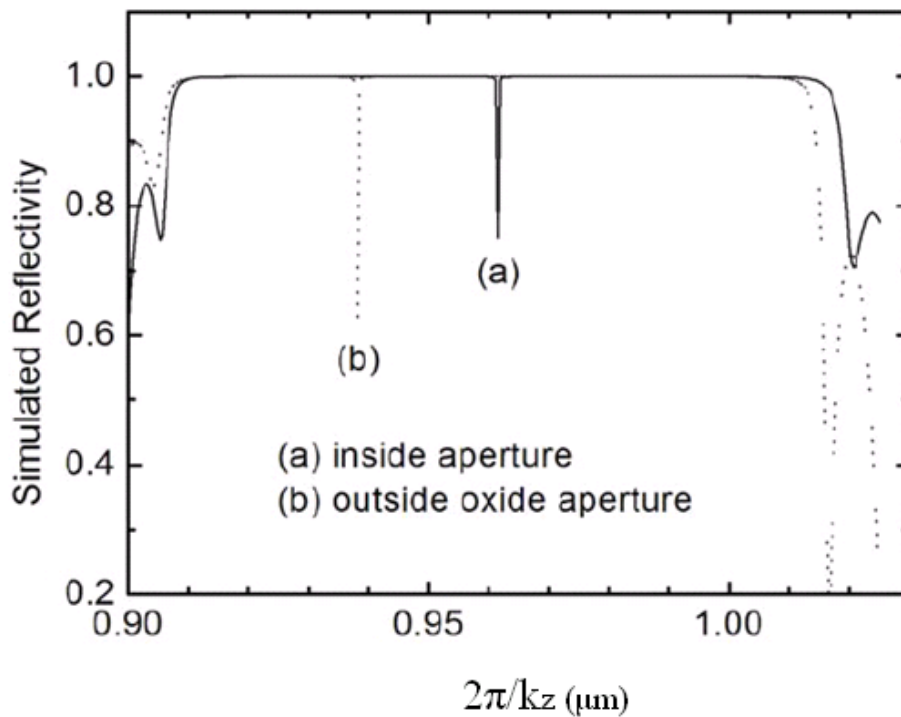
Figure 3.4 Reflectivity spectrum of a typical VCSEL with native oxide aperture calculated using transmission matrix.

3.1.4 All-epitexial confinement Technology

The motivation for developing an alternative to the native oxide aperture technique comes from several drawbacks. Firstly, the thermal strain and volume shrinkage induced by the wet thermal oxidation may cause reliability problem. This is exactly the reason for the low yield of air-gap DBRs in this research. Secondly, the oxidation rate is very sensitive to the composition and local ambient conditions. Therefore, uniformity across a wafer or from one wafer to another is hard to achieve. This translates to yield losses in volume production. Also, the necessity to expose the sidewall of AlGaAs layer for oxidation requires a non-planar process, which makes the process integration difficult, especially for future optoelectronic integrated circuits. Furthermore, all the problems mentioned above get worse when the devices scale down in size, which limits the application of this technology in smaller micro-device.

In this work, an all-epitexial confinement technology is developed in which the thermal strain is under control. The size of the aperture is lithographically defined with excellent uniformity across the wafer and among different wafers. The minimum size is only limited by the lithography technique and equipment used in processing. Also, the finished devices have a planar surface, which eases the difficulties in further processing and integration.

The mechanism of this all-epitaxial confinement technology stems from the

discussion in the last section regarding the blue-shift principle. According to Equation 3.11,

$k_{z,WG} = \dfrac{\pi m_z}{\sqrt{\varepsilon_{WG}} L_z}$. There are three ways to achieve this blue shift or larger $k_{z,WG}$: (1)

decreasing $\varepsilon_{WG;}$ (2) decreasing L_z; (3) increasing m_z while lengthening L_z, accordingly. The

oxide aperture technique falls into the first category. The second and third approaches can

be realized using the MBE regrowth technique, as demonstrated in this work.

Figure 3.5 illustrates the cross section of a VCSEL with a regrowth-defined aperture

design based on method (2) above. The decreased L_z in the cladding region is realized by

interrupting the MBE growth in a strategically selected layer. Then the aperture size is

defined by lithography after it is unloaded from MBE growth chamber. The step selectively

etches away one layer in the cladding region. The device is carefully cleaned and reloaded

back into the MBE chamber. Figure 3.6 shows the calculated reflectivity spectrum of this

design. Photoluminescence spectrum is also shown in the plot. A blue-shift in the vertical

resonant wavelength is achieved as designed. We can expect lateral optical confinement

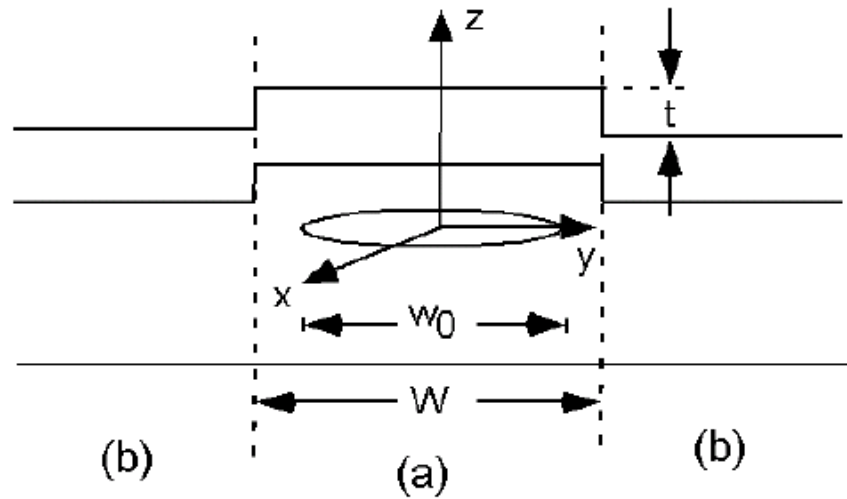from such a structure, just as in oxide aperture.

Figure 3.5 Schematic of a regrowth-defined optical aperture. The cavity length is longer in the aperture region than cladding region.
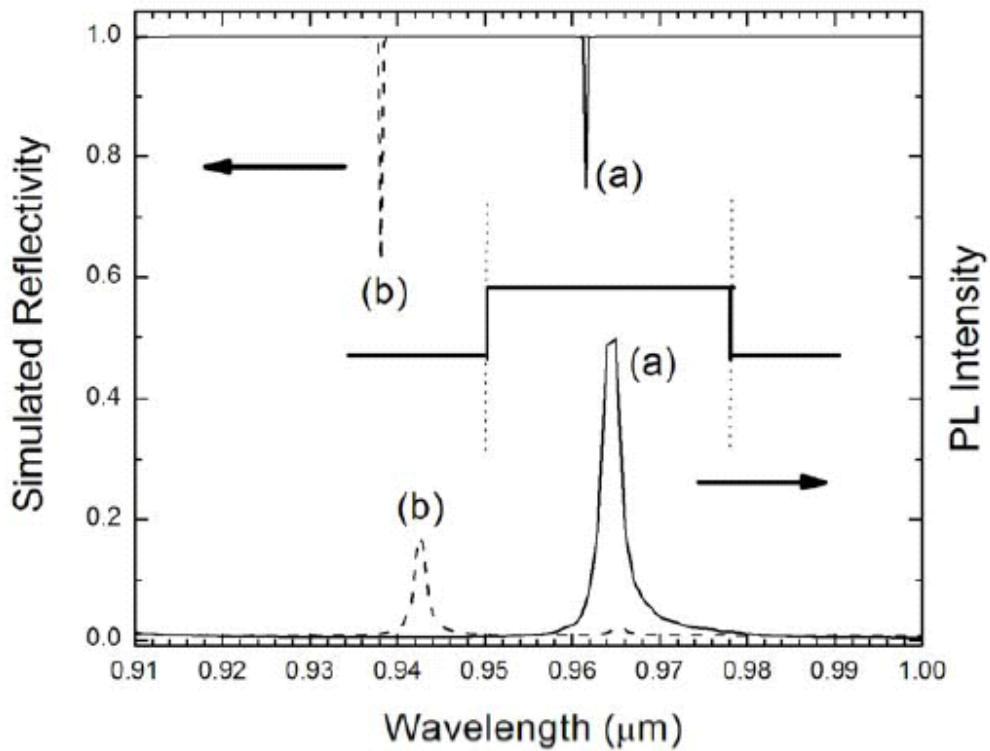

Figure 3.6 calculated reflectivity and measure photoluminescence spectrum. (a) is aperture region and (b) is cladding layer with a layer etched away.

69

Based on method (3), one VCSEL can be designed with even longer L_z in the cladding region, given that a higher order m_z is satisfied for the vertical resonant condition. Figure 3.7 illustrates such a design. In this design, a recessed region is defined in the center,
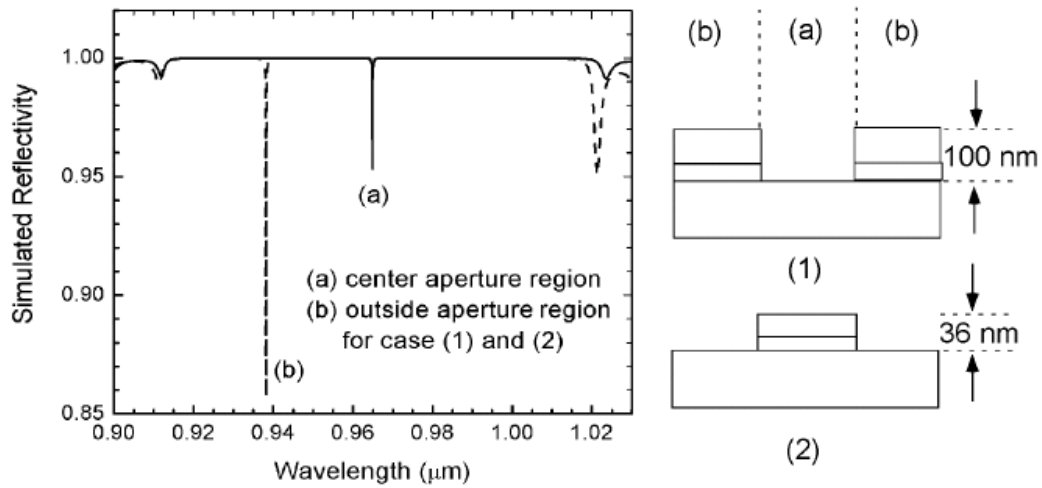
Figure 3.7 Structure designed based on method (3), recess version, and its reflectivity spectrum. An *equivalent* design based on method (2), pillar version, and its reflectivity curve is also shown.

instead of a pillar, as in method (2) designed. The reflectivity spectrum with a 36nm pillar and a 100nm recess are simulated. They achieved the same blue shift in the cladding region, thus they are equivalent in terms of lateral optical confinement. This can be understood as below:

$$
k_z = \frac{2\pi}{\lambda} = \frac{\pi m_z}{nL_z}
$$
$$
\Rightarrow L_z = \frac{\lambda}{2n} m_z \Rightarrow \frac{dL_z}{dm_z} = \frac{\lambda}{2n}
$$

Equation 0.15

Applying the parameters of the design into Equation 3.15, ($\lambda = 940$nm, $n_{average} = 3.45$), we

70

get dL_z/dm_z=136nm. This simple calculation shows that a 136nm longer cavity length is equivalent to raising the resonance to one higher order m_z, while the vertical resonant wavelength remains the same.

The advantage of this method is that it leaves room in the cladding region where for inserting a current blocking layer. Therefore, both the lateral current and optical confinement can be realized with the same structure. Figure 3.8 illustrates a design combining the current and optical confinement. A reversed p-n junction and a low-temperature grown AlGaAs (LTG-AlGaAs) are inserted into the cladding region. The high resistivity of AlGaAs has been researched for a long time[48]. The turn-on voltage with and without the current blocking layers is compared in Figure 3.9 The much higher turn-on voltage in curve (b) indicates that the current-blocking is working well.

This recess design was successfully integrated with air-gap DBRs and eventually led to the demonstration of the first GaAs/air-gap DBR VCSEL.
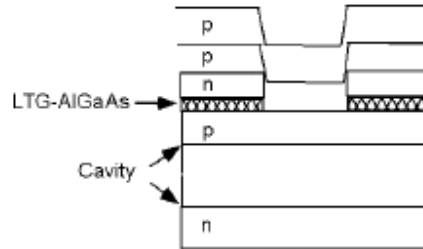
Figure 3.8 A recess version design of confinement. Reversed p-n junction and low temperature grown AlGaAs (LTG-AlGaAs) layer is inserted for current blocking in the cladding region.
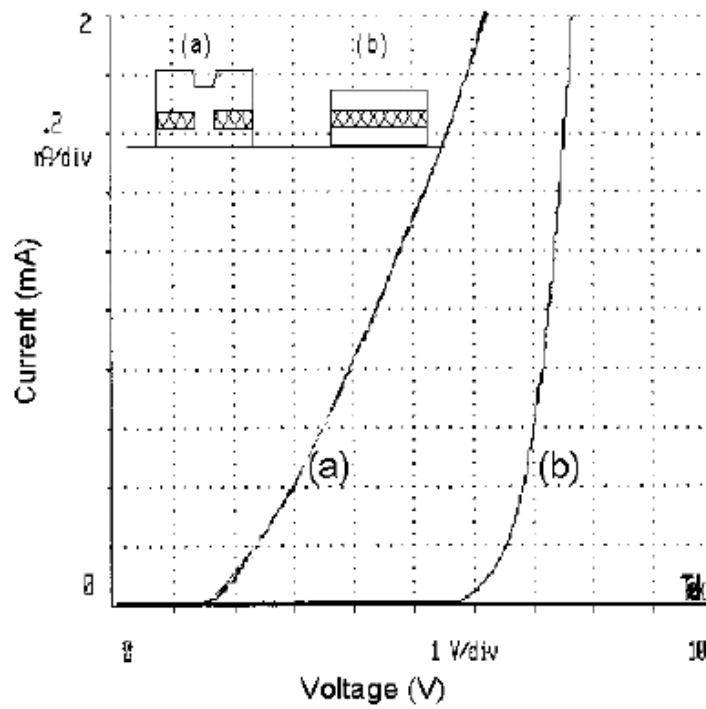
Figure 3.9 I-V curves of device regions (a) with and (b) without current-blocking layer. (b) shows much higher turn-on voltage, indicating the effectiveness of the current blocking.

3.2 Process Flow and Integration

Air-gap DBRs and all-epitaxial confinement are designed, fabricated and tested separately as discussed previously. By combining these two techniques, air-gap VCSELs were realized and lasing operation was successfully demonstrated.

3.2.1 Device Structure
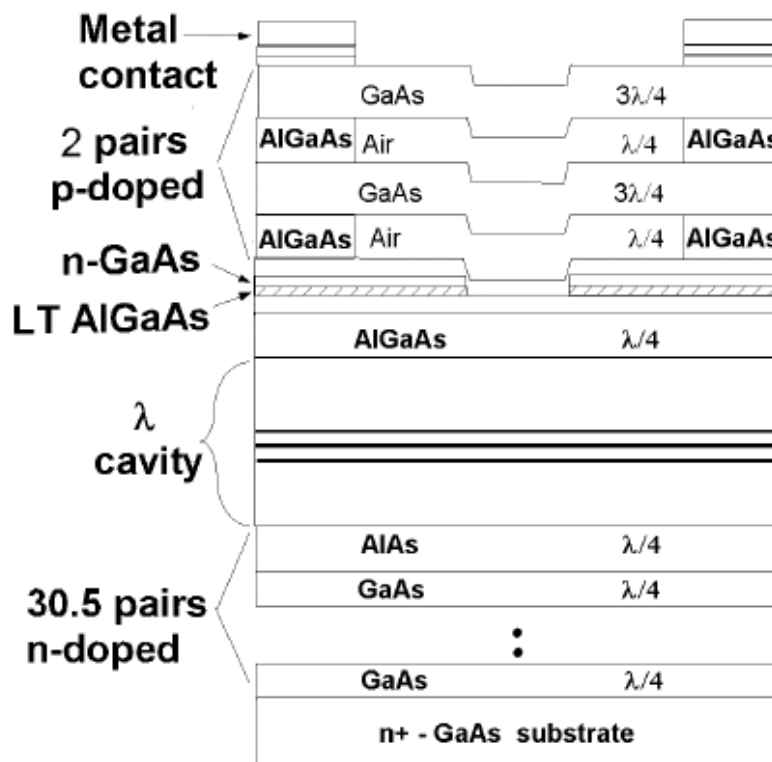
Figure 3.10 VCSEL structure designed to integrate air-gap DBR. All-epitaxial recess confining aperture is incorporated.

The VCSEL structure is designed to integrate air-gap DBR and all-epitaxial recess confining aperture. An N^+ GaAs substrate is used to simplify the current injection scheme. The Bottom DBR employs 30.5 pairs of GaAs/AlAs. Three 6-nm-thick $In_{0.2}Ga_{0.8}As$ quantum wells are embedded as active region in a full wavelength cavity spacer. They are separated from each other with a 10nm GaAs barrier layer. Recess aperture structure is inserted after a quarter wavelength of AlGaAs is grown. Two or three pairs of air-gap DBRs are used as top mirrors. Metal ring contacts are patterned on the wafer surface.

3.2.2 Process Flow

Figure 3.11 illustrates the process flow for an air-gap DBR based VCSEL. The whole process can be divided into four steps: (1) first part growth; (2) confinement aperture definition; (3) second part regrowth; (4) air-gap micromachining

First part growth

The process starts with MBE growth on an N doped GaAs substrate. After the growth of 31 pairs of n-type GaAs/AlAs bottom DBRs, one full wavelength cavity spacer with a quantum well active region embedded inside, and a quarter wavelength p-type AlGaAs layer, a 20 nm p-type GaAs layer is grown and the substrate temperature is decreased to 280°C. A 20 nm thick undoped AlGaAs layer is grown at this low temperature and substrate temperature is raised back to 590°C. This temperature is held for 15 minutes to anneal the LTG-AlGaAs. This is critical for achieving highly resistive LTG-AlGaAs. The

80nm n-type ($2e18$ cm^{-3}) GaAs layer is then grown for the formation of a reversed PN junction. A low temperature InAs protective layer is grown before the first part growth is completed.

Aperture definition

After finishing the first part growth, the wafer is pulled out of MBE chamber. A 10μm hole pattern is formed by standard photolithography. The InAs protective layer and 80nm n-type GaAs layer are selectively etched away using (citric acid + H_2O_2). The photoresist is then removed by oxygen plasma and the LTA-AlGaAs is removed with diluted HF (1:10).

Second part regrowth

Both oxygen plasma and diluted HF are effective and necessary methods for cleaning the wafer before they are reloaded back into the MBE chamber. The InAs protection layer is then thermally etched away by controlling the temperature and Arsenic flux rate. The optimum temperature scheme and Arsenic flux rate are found by careful calibration[49]. After the growth of a p-type GaAs layer to finish the formation of the reversed PN junction, two or three pairs of GaAs/$Al_{0.8}Ga_{0.2}As$ layers are grown. This completes the MBE growth for the entire structure.

Air-gap DBR micromachining

After the wafer is unloaded from the MBE chamber, a ring P-metal (200Å Cr/800Å Au) is deposited with the probing pad on one end. The mesa is also defined by unselective wet etch ($H_2SO_4+H_2O_2+H2O$) for electrical isolation. The type I air-gap discussed in Chapter 2.4 is used in this device. A two-step etch is performed. The first RIE etch defines two rectangular etch-windows (20μmX30μm) with a 15μm separation from each other. The sidewalls of the AlGaAs sacrificial layers are also exposed. $HCl:H_2O$ selective undercutting is carried out to remove the sacrificial layer with 0.8μm/minute etch rate. The wafer is then rinsed and dried with critical point drying, as discussed in chapter 2.4. This concludes the processing of the air-gap VCSEL.

Figure 3.12 shows a SEM picture of air-gap VCSEL after all the processing completed. A color picture of the top view, Figure 3.13, is also shown in which the crystallographic undercut shadow clearly reveals that the air-gaps are formed, and the uniform color of the shadow indicates the flatness of the air-gaps. The small ring in the center shows the location of the confinement aperture formed by all-epitaxial regrowth. The flatness of the air-gaps is also confirmed by a side view of the devices taken by SEM in Figure 3.14. These devices demonstrated low threshold CW lasing at room temperature. Their performance will be analyzed and discussed in next section.
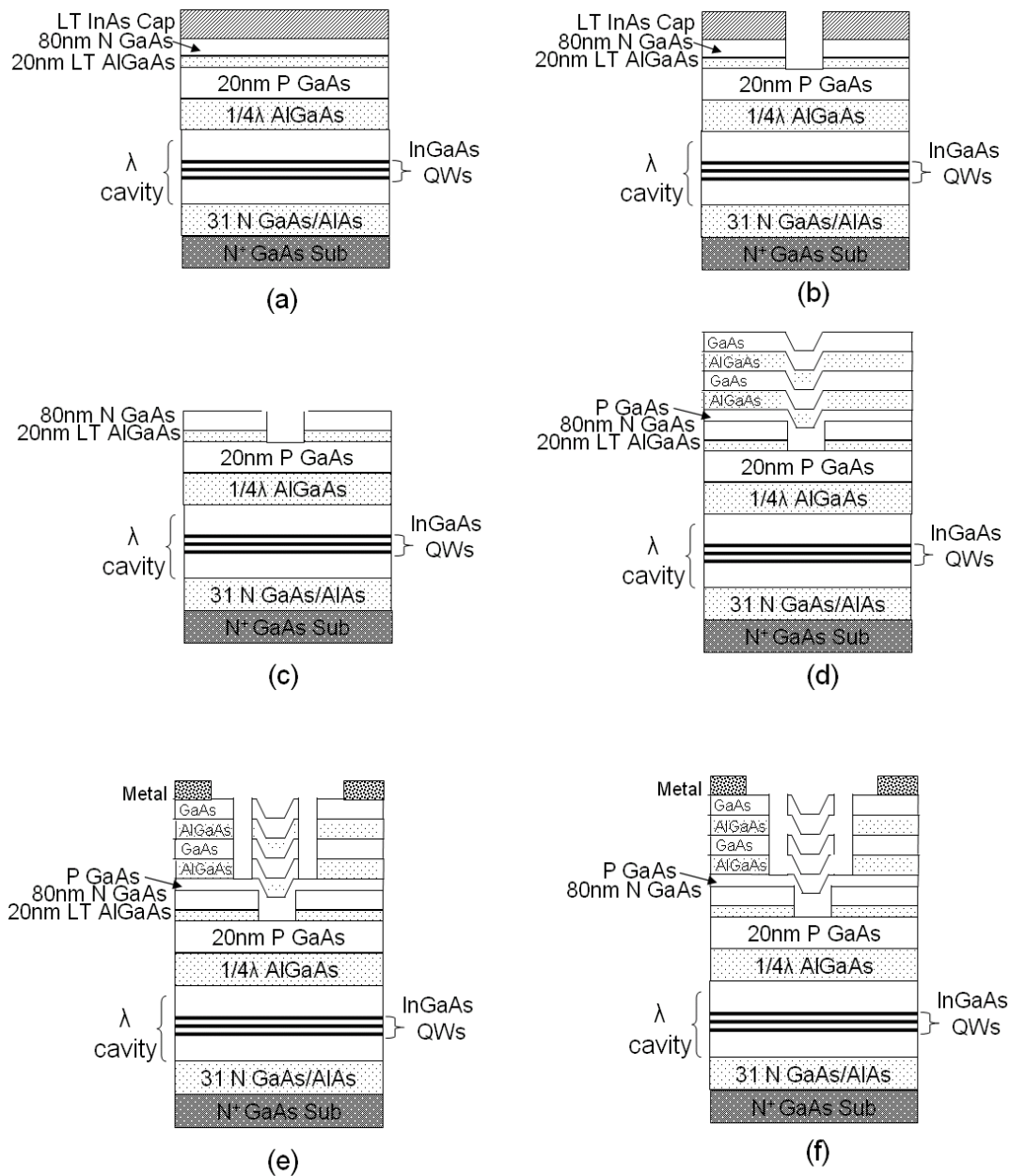
Figure 3.11   Process flow of air-gap VCSEL. (a) First part growth with LTG-InAs protection layer. (b) Recess aperture defined by selective wet etching. (c) After careful cleaning, wafer is loaded into MBE again and InAs is thermally etched away. (d) Top 2 or 3 GaAs/AlAs pairs are re-grown. (e) p-metal is formed. Mesa is etched. Air-gap etch-windows defined by RIE. (f) AlGaAs sacrificial layers are selectively etched away by $HCl:H_2O(1:1)$. Air-gap DBR is rinsed and dried using critical point drying.
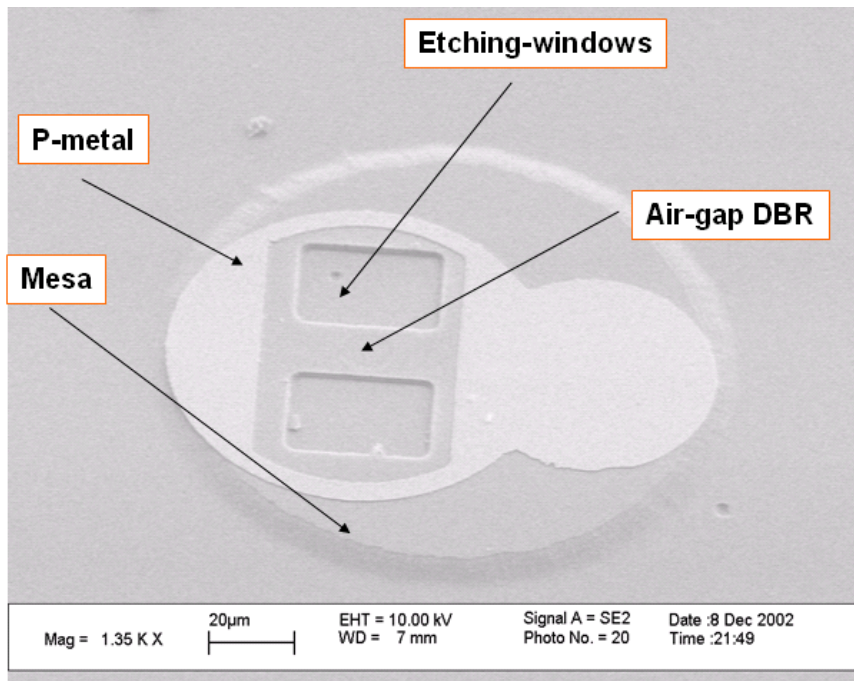
Figure 3.12   Air-gap VCSEL after processing completed
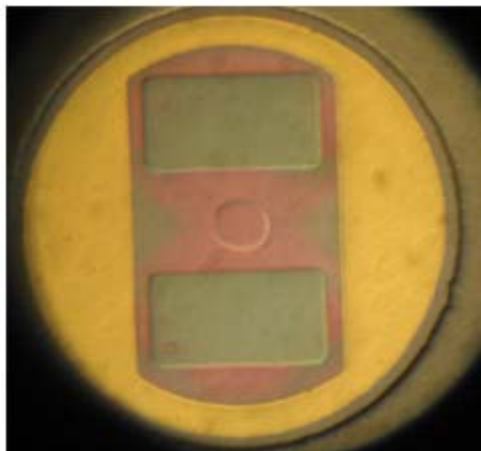
Figure 3.13   Top view of a air-gap VCSEL. The crystallographic shadow shows the formation of air-gaps and the circle in the center reveals the position of regrowth aperture.
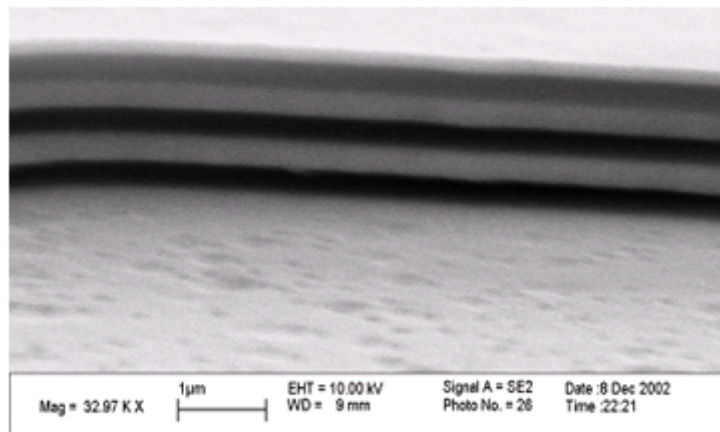
Figure 3.14   Side view of an air-gap VCSEL top DBRs shows the flatness

3.3 Device Demonstration

Two types of air-gap VCSELs are fabricated. One has two pairs of GaAs/air-gap top DBR and the other has three. Both are tested at room temperature with continuous wave electrical pumping. As shown in Figure 3.15, the device with 2 pairs of GaAs/air-gap DBRs starts lasing at a threshold of 1mA, corresponding to a threshold density of 1.27kA/cm^2. Lasing spectrum is also presented, which indicates a lasing wavelength of 9655Å. The output power saturates at 1.4mW with a 9mA injection current. We attribute this saturation to the failure of the current blocking. According to Figure 3.9, the applied voltage increases to 6V when a 2mA current is injected into the device, and the cladding region with the LTG-AlGaAs layer plus reversed PN junction, starts turning on at this voltage. This means that we are pumping the laser together with the cladding region, which greatly reduces the efficiency and eventually leads to the

79

output saturation. A 22% differential quantum efficiency is derived from the L-I curve.

Devices with 3 pairs of air-gap DBRs are also tested at room temperature and demonstrated CW lasing. These devices exhibit a threshold current of 600μA, which corresponds to a current density of 764A/cm^2. The differential quantum efficiency is calculated as 5% from the L-I curve shown in Figure 3.16. Mirror loss and the loss mechanism will be analyzed in next section.
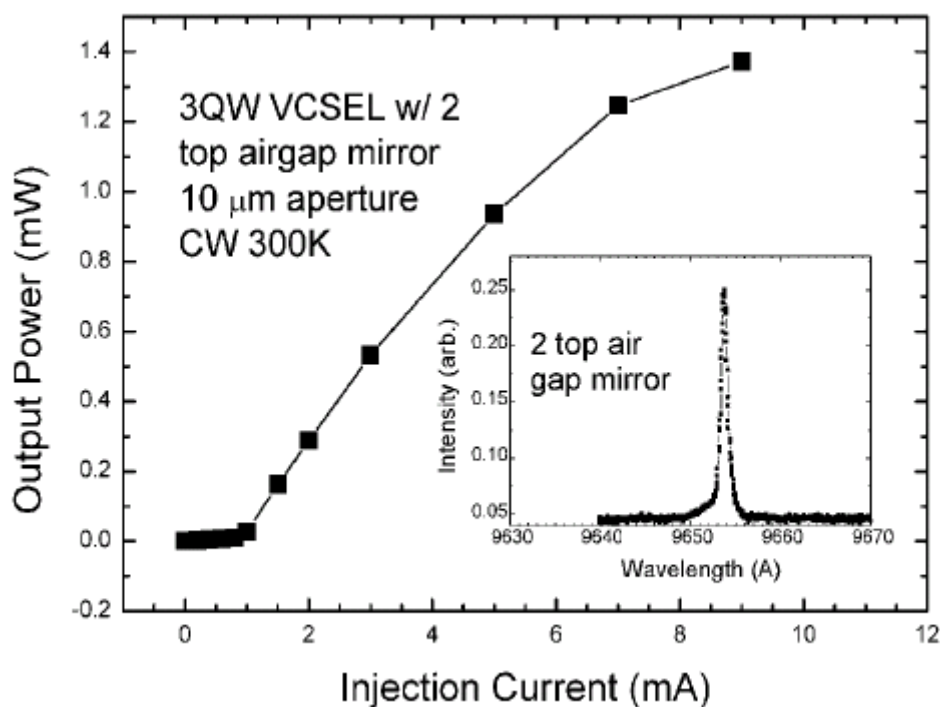
Figure 3.15 L-I curve and lasing spectrum for VCSEL with 2 air-gap DBR
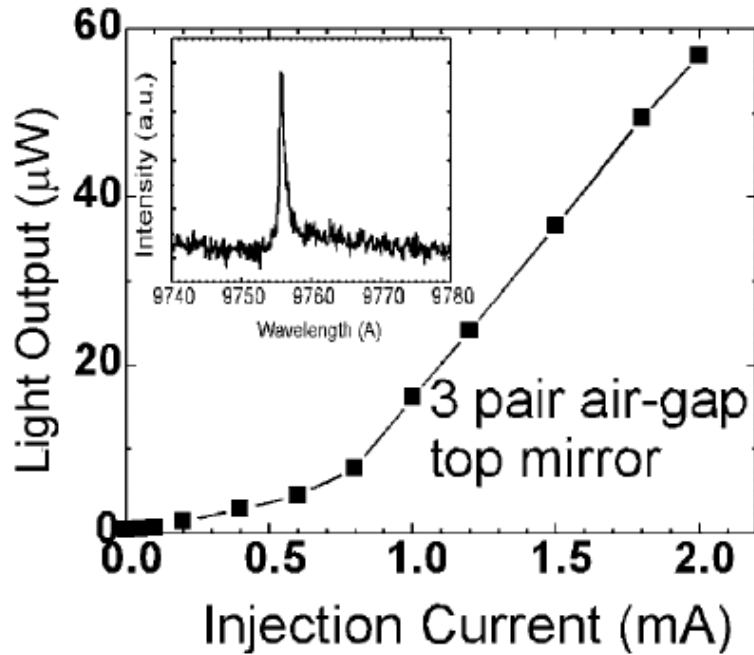
Figure 3.16 L-I curve and lasing spectrum of VCSEL with 3 air-gap top DBR

3.4 Mirror Loss Analysis

The theoretical reflectivity of a 2-pair and 3-pair air-gap DBR are 0.9927 and 0.9994, respectively, based on transmission matrix calculations. The differential efficiency drops from 22% to 5% when the air-gap DBR increases from 2 pairs to 3 pairs, which is associated with optical losses of the air-gap structures. Considering the top mirror output only, we can write the classic expression of differential efficiency as:

$$\eta_d = \eta_i \frac{T_{top}}{\alpha_i + \alpha_{top} + \alpha_{bottom} + T_{top} + T_{bottom}}$$ Equation 3.16

81

Since we are trying to extract the equivalent absorption of a lossy mirror, it is advantageous to write the mirror related photon loss explicitly as those photons escaping from the cavity as output (T_{top}, T_{bottom}) and those lost inside the DBR (α_{top}, α_{bottom}). The internal DBR loss could be anything causing the photon lost from the lasing mode, such as absorption, scattering or diffraction. We expect $\alpha_i \ll \alpha_{top}$ and α_{bottom}, although this will overestimate the air-gap mirror loss. Equation 3.16 can then be simplified for 2 and 3 pair DBR devices as:

$$\eta_{d,2} = \eta_i \frac{T_{top,2}}{\alpha_{top,2} + \alpha_{bottom} + T_{top,2} + T_{bottom}}$$

Equation 3.17

$$\eta_{d,3} = \eta_i \frac{T_{top,3}}{\alpha_{top,3} + \alpha_{bottom} + T_{top,3} + T_{bottom}}$$

Equation 3.18

Then the ratio of these two differential efficiencies can be expressed as:

$$\frac{\eta_{d,2}}{\eta_{d,3}} = \frac{T_{top,2}}{T_{top,3}} \frac{\alpha_{top,3} + \alpha_{bottom} + T_{top,3} + T_{bottom}}{\alpha_{top,2} + \alpha_{bottom} + T_{top,2} + T_{bottom}}$$

Equation 3.19

We assume that η_i, α_{bottom}, and T_{bottom} do not change when the DBR changes from 2 pairs to 3 pairs. We also assume that the mirror internal loss is uniformly distributed, which makes it possible to compare with research data in the literatures. Figure 3.17 is a plot of the $\eta_{d,2}/\eta_{d,3}$ ratio versus distributed air-gap mirror loss. Curves with different assumptions for bottom DBR loss (0, 5cm^{-1}, 10cm^{-1} and 15cm^{-1}) are plotted. The distributed loss of the air-gap is then extracted as 160cm^{-1}, 106cm^{-1}, 55cm^{-1} and 0cm^{-1}, respectively. It is reasonable to take the value of 5cm^{-1} for the bottom DBR, considering

the doping level 5×10^{17}cm^{-3} and the value found in the literatures, which lead to a distributed loss of 106cm^{-1} for the air-gap DBR. This number is higher than expected. Part of the reason is that the internal optical loss is ignored in the calculation. Those losses are in fact attributed to air-gap DBR loss. Thus, if they are comparable to the internal DBR losses, it will lead to a substantial overestimation in mirror loss. In fact, based on the device design and processing for these devices, the loss is most likely overestimated.
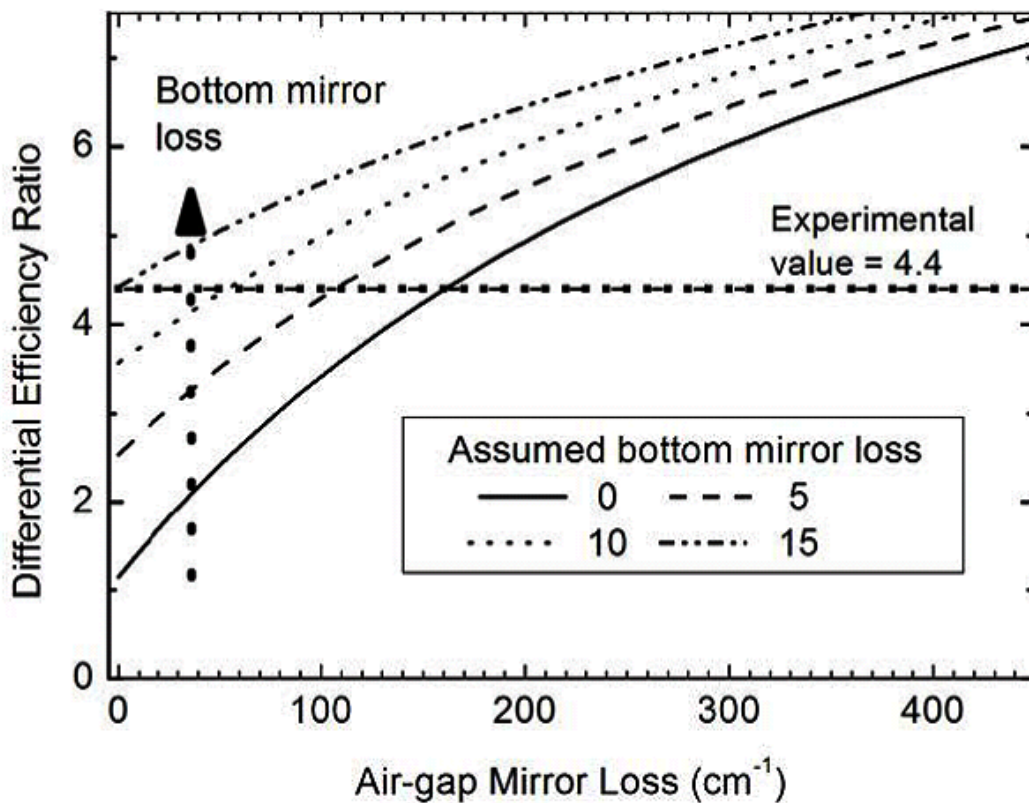

Figure 3.17 $\eta_{d,2\text{-pair}}/\eta_{d,3\text{-pair}}$ versus air-gap mirror loss. Four curves are plotted based on different bottom semiconductor mirror loss assumption. The horizontal line shows the experiment value of the differential efficiency ratio

First, as illustrated in Figure 3.10, this device design adopts a recess aperture for lateral optical and electrical confinement. The optimum design is a pillar structure, in which a small step can ensure good index guiding. Although the simulation shows the 100nm recess design is equivalent to a 36nm step structure, the regrowth quality may greatly change the optical characteristics of the microcavity. The SEM pictures reveal a dramatic difference in step height along the boundary, which may lead to strong anti-guiding effects, instead of guiding effects. This can increase the internal loss significantly, which is attributed to mirror loss in our calculation.

Second, the 100nm height difference between the recess center and the higher cladding region is quite disadvantageous. The first reason for such a high step is to have enough thickness to accommodate the depletion region in the reversed PN junction at the given doping level and at a reasonable operation voltage. The second reason is to achieve the desired blue shift in the vertical resonant wavelength. However, such a high step makes it difficult to control the regrowth quality, especially at the edge. We found crystallographic roughness existing at the edge, which will cause high scattering loss when lasing mode passes the edge region. Also, the high step itself can cause scattering loss even if it is grown perfectly. All these scattering loss are also attributed to the air-gap mirror loss.

Third, although the wet selective etching and CPD drying are optimized to micromachine the air-gap DBR structure, some imperfections may still exist. Direct evidence needs to be collected about the mirror quality in addition to the SEM and

infrared CCD pictures. Laser or white light interferometry can be used to measure the curvature and roughness of the air-gap. These parameters are important information for analyzing the mirror quality and can help correct the estimation of optical loss caused by the mirror.

3.5 Summary

A robust and high yield process flow is developed to integrate air-gap DBRs into VCSELs. Type I air-gap structures which contain multiple GaAs/air-gap stacks, as discussed in Chapter 2, are employed in these devices.

A proper lateral electrical and optical confinement is critical for achieving efficient VCSEL operation. The oxide aperture technology was developed to serve this function. The analysis of the mechanism of oxide aperture led to a more insightful understanding of lateral optical mode confinement. More flexible methods were discovered to provide the same confinement, by realizing an effective blue shift of the vertical resonant wavelength in the cladding region. This blue shift can be obtained by a center pillar structure or a recessed region also according to the theoretical simulation. An all-epitaxial confinement technique is developed based on this theory.

This novel all-epitaxial confinement technique eases process integration due to the well-controlled strain and planar geometry. VCSELs with 2 and 3 pairs of air-gap DBRs were built with this all-epitaxial confinement technique. Room temperature and CW lasing were achieved for both devices. A low threshold of 600μA was

demonstrated with the 3-pair air-gap DBR devices. Differential efficiency decreases from 22% to 5% when the mirrors change from two pairs to three pairs.

A $106cm^{-1}$ distributed loss is extracted from the experimental data. The higher than expected loss is attributed to the diffraction loss resulting from possible anti-guiding effects at the aperture boundary and the scattering loss induced by the rough edge and large step height surrounding the recess aperture. The optical loss can be greatly reduced by a pillar aperture design. In this way, the index-guiding is ensured and a smaller height of step can be used.

The device efficiency and maximum output can be improved significantly by using a more robust current confinement technique. A careful doping profile design and band-gap engineering can also help solve this problem by reducing the operating voltage.

The Author believes that the performance of the air-gap VCSELs can be greatly improved by doing above modifications.

Chapter 4

Summary

Distributed Bragg reflectors (DBR) are an essential part of VCSEL devices. Low loss and high reflectivity DBRs are conventionally obtained by growing alternating semiconductor layers on a substrate. Crystal lattice match is required to avoid a high misfit dislocation density. This limits the material choice, especially when combining other requirements, such as large refractive index. The absence of a suitable DBR has been a major hurdle for VCSEL development. Air-gaps provide the largest achievable refractive index contrast with semiconductor materials and can be made from any pair of materials, as long as a highly selective etching is available. This material flexibility and its merits as a high quality mirror make air-gap DBRs a key technology for VCSEL development. Other applications for air-gap structures include MOEM systems, microcavity physics and device research.

This dissertation focuses on the development of air-gap VCSELs, from concept to demonstration of working devices on the GaAs material system.

Air-gap DBRs are simulated by solving the transmission matrix formulas of Maxwell's equations. Reflectivity higher than 0.999 and an ultra-wide stop-band can be obtained at 1.3μm with just 3 pairs. Comparisons are made with other current DBR technology and show evident advantage for air-gap DBR.

Two types of air-gap DBR structures are proposed. One contains multiple GaAs/air-gap stacks, and the other is a hybrid mirror combining one air-gap structure with dielectric and metal reflectors. Both mirrors are analyzed using the transmission matrix method and show very high reflectivity with a small total thickness.

The principle obstacle of making air-gap structure is stiction problem, which is caused by the surface tension of a diminutive liquid between suspended films when the devices is exposed to rinsing and drying. Different techniques were approached to deal with stiction based on the understanding of the origin and physics of this problem. In the first structure with multiple semiconductor/air-gap stacks, a critical point drying technique was employed to counteract the problem. For the second structure consisting of hybrid mirrors, a combination of five silver posts and one silver top disk were used to provide the necessary mechanical support to withstand the capillary force induced by liquid surface tension. Both structures with good quality were demonstrated.

Process integration was hindered by the wet thermal oxidation during development. The thermal strain and volume shrinkage induced by wet thermal oxidation make it difficult to build high quality air-gap mirrors on top of the structure. This thermal process also makes the sacrificial layer etching less controllable and predictable. All of these result in a challenging process integration and poor overall yield. Unfortunately, the lateral electrical and optical confinement offered by the oxide aperture is an indispensable mechanism for efficient VCSEL lasing operation.

This mechanism was analyzed using a simple 3-D optical mode confinement model, which led to a more general understanding that blue shifting of the vertical resonance is the cause to the confinement. This theory is also confirmed by experiments and an effective index theory developed by other researchers. Based on these theoretical analyses, an all-epitaxial technique was developed. Basically, the blue-shift of the cladding region can be obtained, not only by a change in average index, but also by a change in effective cavity length. Both recess and pillar aperture designs were analyzed using transmission matrix methods, and their effectiveness was confirmed. In this research, the recess aperture is adopted because it leaves space for the insertion of a current blocking structure. A reversed PN junction and a highly resistive LTG-AlGaAs layer are used to confine the injected current inside the center aperture. This aperture is formed by selective wet etching after interrupting the MBE growth. Regrowth is performed to finish the device epitaxy. By replacing the oxide aperture with the regrowth aperture, process integration is simplified. A robust and high yield process flow is eventually developed for air-gap VCSELs.

CW and room temperature lasing is demonstrated for devices with two and three pair top GaAs/air-gap DBRs. When the DBR changes from 2 to 3 pairs, the threshold decreases from 1mA to 600μA, while the differential efficiency drops from 22% to 5%. A 1.4mW maximum power output is achieved, which is limited by the failure of current blocking. A distributed loss of ~100cm^{-1} is extracted from the experimental data. The cause of this loss is believed to originate in scattering loss from the high

aperture step and rough regrowth edge. Possible strong anti-guiding effects at the boundary also contribute to the total optical loss. Therefore, there is much room for device improvement by eliminating or reducing these optical losses. A small step pillar aperture is more advantageous for optical loss control. With the combination of a better optical aperture and a more robust current blocking structure, device performance can be greatly improved in many aspects.

In conclusion, this research demonstrates that air-gap DBRs are a feasible alternative to current DBR technology. The advantages of air-gap DBRs will enable the development of VCSELs in different spectrum.

References

1. H. Soda, K. Iga, C. Katahara, and Y. Suematsu, "Surface-emitting injection lasers," Jpn. J. Appl. Phys., vol. 18, pp. 2329–2330, 1979.

2. Kenichi Iga, "Surface-Emitting Laser—Its Birth and Generation of New Optoelectronics Field", IEEE Journal of Selected Topics in Quantum Electronics, vol. 6, no. 6, pp. 1201, 2000.

3. Jim A. Tatum and James K. Guenter, " The VCSELs are coming", Proceedings of SPIE, vol. 4994, pp. 1-11, 2003.

4. V. Michael Bove, Jr. and Wilfrido Sierra, "Personal Projection, or How to Put a Large Screen in a Small Device", Proc. SID 2003.

5. D. L. Huffaker, D. G. Deppe, K. Kumar, and T. J. Rogers, "Native-oxide defined ring contact for low threshold vertical-cavity lasers," Appl. Phys. Lett., vol. 65, pp. 97–99, 1994.

6. D. L. Huffaker, J. Shin, and D. G. Deppe, "Low threshold half-wave vertical-cavity lasers," Electron. Lett., vol. 30, pp. 1946–1497, 1994.

7. http://www.picolight.com/Release29.asp, "Picolight introduces 1310nm VCSEL Transceivers", August, 5, 2003.

8. V M Ustinov, A E Zhukov, A R Kovsh, S S Mikhrin, N A Maleev, B V Volovik, Yu G Musikhin, Yu M Shernyakov, E Yu Kondat'eva, M V Maximov, A F

Tsatsul'nikov, N N Ledentsov, Zh I Alferov, J A Lott and D Bimberg, "Long-wavelength quantum dot lasers on GaAs substrates", 2000 Nanotechnology, 11, 397-400.

9. N. Samal, Y. Cao, D. Ding, J. Wang, S. Yu, X. Jin, S. Chaparro, Y. Sadofyev, S. R. Johnson, Y. Zhang, "Room temperature CW operation of long wavelength GaAsSb/GaAs VCSELs grown on GaAs", Proceedings of SPIE Vol. 4994.

10. Anan, T.; Yamada, M.; Nishi, K.; Kurihara, K.; Tokutome, K.; Kamei, A.; Sugou, S., "Continuous-wave operation of 1.30μm GaAsSb/GaAs VCSELs", Electronics letters, vol.37, pp. 566-567, 2001.

11. Jayaraman, V.; Geske, J.C.; MacDougal, M.H.; Peters, F.H.; Lowes, T.D.; Char, T.T., "Uniform threshold current, continuous-wave, singlemode 1300 nm vertical cavity lasers from 0 to 70°C", Electronics Letters, vol. 34, no. 14, pp. 1405-1407, 1998.

12. C. J. Chang-Hasnain, "Tunable VCSEL", IEEE Journal of Selected Topics in Quantum Electronics, vol. 6, no. 6, pp.978, 2000.

13. A.T.T.D. Tran, Y. H. Lo, Z. H. Zhu, D. Haronian, and E. Mozdy, "Surface micromachined Fabry–Perot tunable filter," IEEE Photon. Technol. Lett., vol. 8, pp. 393–395, Mar. 1996.

14. G. L. Christenson, A. T. T. D. Tran, Z. H. Zhu, Y. H. Lo, M. Hong, J.P. Mannaerts, and R. Bhat, "Long-wavelength resonant vertical-cavity LED/photodetector with a 75-nm tuning range," IEEE Photon. Technol. Lett.,

vol. 9, pp. 725–727, June 1997.

15. Purcell E. M. Purcell, "Spontaneous emission probabilities at radio frequencies," Phys. Rev., vol. 69, pp. 681, 1946.

16. H. Huang and D. G. Deppe, "Obtaining high efficiency at low power using a quantum-dot microcavity light emitting diode," IEEE J. Quantum Electron., vol. 36, pp. 674-679, 2000.

17. L. A. Coldren and S. W. Corzine, "Diode Lasers and Photonics Integrated Circuits", Wiley, New York, 1995.

18. C. Weisbuch and B. Vinter, "Quantum Semiconductor Structures: Fundamentals and Applications", Academic Press, 1991.

19. Michael H. MacDougal, P. Daniel Dapkus, Aaron E. Bond, Chao-Kun Lin, and Jon Geske, "Design and Fabrication of VCSEL's with Al_xO_y–GaAs DBR's", IEEE Journal of Selected Topic In Quantum Electronics, vol. 3, no. 3, pp. 905, June 1997.

20. Adil Karim, Staffan Björlin, Joachim Piprek, John E. Bowers, "Long-Wavelength Vertical-Cavity Lasers and Amplifiers", IEEE JOURNAL ON SELECTED TOPICS IN QUANTUM ELECTRONICS, vol. 6, no. 6, 2000.

21. D. L. Huffaker, L. A. Graham, H. Deng, and D. G. Deppe, "Sub-40 A continuous-wave lasing in an oxidized vertical-cavity surface-emitting laser with dielectric mirrors," IEEE Photon. Technol. Lett., vol. 8, pp. 974–976,

1996.

22. D. I. Babic, T. E. Reynolds, E. L. Hu, and J. E. Bowers, "In situ characterization of sputtered thin films using a normal incidence laser reflectometer," J. Vacuum Sci. Technol. A, pt. 1, vol. 10, no. 4, pp. 939–944, 1992.

23. S. Uchiyama, N. Yokouchi, and T. Ninomiya, "Continuous-wave operation up to 36 degrees C of 1.3- m GaInAsP-InP vertical-cavity surface-emitting lasers," IEEE Photon. Technol. Lett., vol. 9, pp. 141–142, 1997.

24. H. Soda, K. Iga, C. Kitahara, and Y. Suematsu, "GaInAsP/InP surface emitting injection lasers," Jpn. J. Appl. Phys., vol. 18, pp. 2329–2330, Dec. 1979.

25. Alley R L, Cuan G J, Howe R T and Komovopoulos K, "The effect of release-etch processing on surface microstructure stiction", Proc. IEEE Solid-State Sensor and Actuator Workshop, pp 202–7, 1992.

26. Legtenberg R, Elders J and Elwenspoek M, "Stiction of surface micromachined structures after rinsing and drying: model and investigation of adhesion mechanisms" Proc. Int. Conf. on Solid-State Sensors and Actuators (Transducers '93, Yokohama) pp 198–201, 1993.

27. Mastrangelo C H and Hsu C H, "Mechanical stability and adhesion of microstructures under capillary forces", J. Microelectromech. Syst. 2 33–55, 1993.

28. Alley R L, Mai P, Komovopoulos K and Howe R T, "Surface roughness

modification of interfacial contacts in polysilicon microstructures", Proc. Int. Conf. on Solid-State Sensors and Actuators (Transducers '93, Yokohama), pp 288–91, 1993.

29. Scheeper P R, Voorthuyzen J A, Olthuis W and Bergveld P, "Investigation of attractive forces between PECVD silicon nitride microstructures and an oxidized silicon substrate Sensors Actuators A", 30, 231–9, 1992.

30. Guckel H, Sniegowski J J, Christenson T R, Mohney S and Kelly T F, "Fabrication of micromechanical devices from polysilicon films with smooth surfaces Sensors Actuators", 20, 117–22,1989.

31. J. W. Lee, M. W. Devre, B. H. Reelfs, D. Johnson, J. N. Sasserath, F. Clayton, D. C. Hays and S. J. Pearton, "Advanced Selective Dry Etching of GaAs/AlGaAs in High Density Inductively Coupled Plasmas" J. Vac. Sci. Technol., A, 18, 1220 (2000).

32. N. Takeshima, K.J. Gabriel, M. Ozaki, J. Takahasji, H.Horiguchi and H. Fujita, Electrostatic Parallelogramactuators. Proc. 6th. Int. Conf., Solid-State Sensors and Actuators (Transducers' 91), San Francisco, CA, USA, June 24-28, pp. 63-66, 1991.

33. M. Orpana and A.O. Korhonen, "Control of residual stress of polysilicon thin films by heavy doping in surface micromachining", Proc. 6th. Int. Conf., Solid-State Sensor and Actuator (Transducers' 91), San Francisco, CA, USA, June 24-28, 1991, pp. 957-960.

34. R.A. Brennen, M.G. Lim, A.P. Pisano and A.T. Chou., "Large displacement linear actuator", Proc. IEEE Solid State Sensors and Actuators Workshop, Hilton Head island, SC, USA, June 4-7, pp. 135-139, 1990.

35. F.S.A. Sandejas, R.B. Apte, W.C Banyai and D.M. Bloom, "Surface Microfabrication of Deformable Grating Light Valves for High Resolution Displays", Proc. 7th. Int. Conf., Solid-State Sensors and Actuators (Transducer 93), Yokohomo, Japan, Abstr. late news papers, pp. 6-7, June 7-10, 1993.

36. R.L. Alley, P. Mai, K. Komvopoulos and R.T. Howe, "Surface Roughness Modification of Interfacial Contact in Polysilicon Microstructures," Proc. 7th Int. Conf., Solid-State Sensors and Actuators (Transducers '93), Yokohama, Japan, June 7-141993, pp. 288-291, 1993.

37. Rob Legtenberg, Harrie A.C. Tilmans, Job Elders and Miko Elwenspoek, "Stiction of surface micromachined structures after rinsing and drying: model and investigation of adhesion mechanisms", Sensors and Actuators A, 43, 230-238, 1994.

38. www.quorumtech.com

39. Jong-Hee Kim, Dae Ho Lim, and Gye Mo Yang, "Selective Etching of AlGaAs/GaAs Structures Using the Solutions of Citric Acid/H_2O_2 and De-ionized H2O/buffered Oxide Etch", J. Vac. Sci. Technology. B 16(2), 1998.

40. Kent D. Choquette, Kent M. Geib, Carol I. H. Ashby, Ray D. Twesten, Olga Blum, Hong Q. Hou, David M. Follstaedt, B. Eugene Hammons, Dave Mathes,

and Robert Hull, "Advances in Selective Wet Oxidation of AlGaAs Alloys", IEEE Journal of Selected Topic in Quantum Electronics, vol. 3, no. 3, June 1997.

41. Q. Deng and D. G. Deppe, "Spontaneous emission coupling from multiemitters to the quasimode of a planar cavity," Phys. Rev. A, vol. 53, pp. 1036–1047, 1996.

42. D. L. Huffaker, D. G. Deppe, K. Kumar, and T. J. Rogers, "Native-oxide defined ring contact for low threshold vertical-cavity lasers," Appl. Phys. Lett., vol. 65, pp. 97–99, 1994.

43. T.-H. Oh, "Control of Lateral Diffraction Loss in Vertical Cavity Surface Emitting Lasers", Dissertation, 1998.

44. C. C. Hansing, H. Deng, D. L. Huffaker, D. G. Deppe, B. G. Streetman, and J. Sarathy, "Low-threshold continuous-wave surface-emitting lasers with etched-void confinement," IEEE Photon. Technol. Lett., vol. 6, pp. 320–322, 1994.

45. Dennis G. Deppe, Diana L. Huffaker, Tchang-hun Oh, Hongyu Deng, and Qing Deng, "Low-Threshold Vertical-Cavity Surface-Emitting Lasers Based on Oxide-Confinement and High Contrast Distributed Bragg Reflectors", IEEE Journal of Selected Topic in Quantum Electronics, vol. 3, no. 3, pp. 893, 1997

46. D. G. Deppe, T.-H. Oh, and D. L. Huffaker, "Eigenmode confinement in the

dielectrically apertured Fabry–Perot microcavity," IEEE Photon. Technol. Lett., vol. 9, pp. 713–715, June 1997.

47. G. R. Hadley, "Effective index model for vertical-cavity surface-emitting lasers," Opt. Lett., vol. 20, pp. 1483–1485, 1995.

48. M. R. Melloch, J. M. Woodall, and E. S. Harmon, "Low-temperature grown III-V materials," Annu. Rev. Mater. Sci., vol. 25, pp. 547-600, 1995.

49. Hao Chen, "GaAs Based Apertured Vertical Cavity Surface Emitting Lasers and Microcavity Light Emitting Diodes", Dissertation, 2003.

Vita

Qingwei Mo was born in Hechuan, ChongQing, P. R. China on September 25, 1973, the son of Yunda Mo and Shunrong Gao. He entered the Materials Science and Engineering Department of Tsinghua University in 1991 and received his B.E. degree in 1996. From September 1996 to December 1998, he was a graduate student of the Institute of Semiconductors, Chinese Academy of Sciences and received his M.S. degree on semiconductor materials. In January 1999, he entered graduate school in the electrical and computer engineering department at the University of Texas at Austin. In 2003, he was employed as an intern research scientist at Keyotee, Inc in Austin, TX. He received his M.S. degree in December, 2001 and Ph.D. in August 2004.

Permanent address: Yuanda Mo, Hechuan No.1 Middle School, Hechuan, ChongQing,
421520, P.R. China

This dissertation was typed by the author